Solvothermal Synthesis of Bi2s3 Nanoparticles for Active Photocatalytic and Energy Storage Device Applications

C. Sambathkumar
Kalasalingam Academy of Research and Education
V. Manirathinam
Kalasalingam Academy of Research and Education
A. Manikandan (mkavath15@gmail.com)
Bharath Institute of Higher Education and Research https://orcid.org/0000-0001-6513-7428
M. Krishna Kumar
Kalasalingam Academy of Research and Education
S. Sudhakar
Alagappa University
P. Devendran
Kalasalingam Academy of Research and Education

Research Article

Keywords: Bi2S3 Nanoparticles, Bi[DTC] complex, Solvothermal technique, electrochemical studies, Energy storage device, Photodegradation

Posted Date: March 17th, 2021

DOI: https://doi.org/10.21203/rs.3.rs-305914/v1

Version of Record: A version of this preprint was published at Journal of Materials Science: Materials in Electronics on July 16th, 2021. See the published version at https://doi.org/10.1007/s10854-021-06596-w.

Solvothermal synthesis of Bi_2S_3 nanoparticles for active photocatalytic and energy storage device applications

C. Sambathkumar[1], V. Manirathinam[1], A. Manikandan[2], M. Krishna Kumar[1], S. Sudhakar[3], P. Devendran[1]*

[1]Department of Physics, International Research Centre, Kalasalingam Academy of Research and Education, Krishnankoil-626 126, Tamil Nadu, India.

[2]Department of Chemistry, Bharath Institute of Higher Education and Research (BIHER), Bharath University, Chennai - 600 073, Tamil Nadu, India

[3] Department of Physics, Alagappa University, Karaikudi - 630003, Tamil Nadu, India

Email: pdevavenmani@gmail.com, p.devendran@klu.ac.in

Abstract

High edge energy storage with large life-span stable materials have become the most significant and major requirement in near future. Bismuth sulfide (Bi_2S_3) Nanoparticles (NPs) was effectively synthesized by utilizing Bismuth diethyldithiocarbamate (Bi[DTC]) complex as single-source antecedent. The synthesized Bi_2S_3 NPs were affirmed by structural, morphological and thermal analysis with various analytical studies. The electrochemical performance of Bi_2S_3 NPs reveals that, exhibit redox behavior from cyclic voltammetry analysis, the charge-discharge analysis was examined by the galvanostatic chronopotentiometry. Bi_2S_3 NPs exhibit excellent supercapacitor behavior with value of the specific capacitance 470 Fg^{-1} at current density 0.5 Ag^{-1} and the retentivity of 79 % after 1000 cycles. The Bi_2S_3 NPs were further utilized as

photocatalytic discoloration of Congo Red (CR) dye in aqueous medium under UV-light irradiation. Which shows, excellent catalytic behaviour, up to 98% of CR dye degrade within 150 min. and it is exhibit good catalytic stability and reusability.

Keywords**:** Bi_2S_3 Nanoparticles, Bi[DTC] complex, Solvothermal technique, electrochemical studies, Energy storage device, Photodegradation.

1. Introduction

In the recent decade, broad ranging attempts were made to grow use of new phase grid storage system with maximum power and energy density to be used in crossover hybrid car and versatile hardware. Energy storage devices are considered as a promising nominee for securing and conveying a moderately high measure of energy in brief timeframes, indicating magnificent reversibility and lifelong execution [1]. Other than the carbon materials, for example, carbon nanofibers, actuated carbons and graphene oxides change metal mixes, for example, metal sulfides or metal oxides moreover hydroxides are considered as appealing potential terminal equipment for utilize in supercapacitors because of the large-capacitance esteems, which transfer into the upgraded energy density [2–5]. The presentation of the semiconductor materials into the respectable metal nanostructures totally modifies their electronic and optical properties; along these lines, positions them as most chased materials utilized in field impact transistors, photocatalytic response, photo detectors and furthermore in supercapacitors (broadly utilized in buyer and printed hardware, flight, transportation, and related innovations) [6–9]. In meantime; metal sulfides are significant product of semiconductor and have also been utilized to create supercapacitor electrodes [10]. On account of metal sulfides, it has been recognized as a fantastic pseudo capacitive (redox) material at room temperature with its high conductivity and redox

properties. The metal sulfides like, Bismuth sulfide [11], Nickel sulfide [12], Zinc sulfide [13], Cadmium sulfide [14], Cobalt sulfide [15] is proposed with different composite stages and has a widespread scope of energy storage applications [16,17].

Metal sulfides are attractive in wide group of functional materials because of their wide applications within electronic, catalytic, sensor, optics, biomedical sectors and energy storage conversion [18–20] with few synthesis reports are available like, co precipitation, hydrothermal, microwave irradiation and sonochemical techniques [21]. In addition, preparation of Bi_2S_3 NPs by various methods has been employed such as chemical vapor deposition method, electrochemical deposition, sonochemical system, organometallic complex decomposition. Hydrothermal technique has been valid to bismuth sulfide nano ribbons and nanotubes preparation [22]. Bi_2S_3 nanomaterials is a prominent semiconducting material and it has drawn significant interest in nonlinear optical device, thermoelectric device, optical modulators, sensors, and optoelectronic devices, electronics, and well as FT-IR spectroscopy due to its potential applications. Bi_2S_3 (Bismuth sulfide) has a direct band gap semiconductor with a high coefficient of absorption, the larger band gap energy 1.3 to 1.7 eV [23–26]. This material provides possible applications for thermoelectric cooler system as well [10].

In recent days, many researchers concentrate on semiconducting photocatalysts to accomplish the needs regarding organic pollutions, photochemical water splitting technique [27]. Photocatalytic technology is an upcoming growth in oxidation innovation, which uses to stimulate electrons to provide more oxidizing methods. It can mineralize organic molecules into carbon dioxide and water and reduces organic pollutants from water completely [28,29]. Metal sulfides are introduced to gathering a deeply effective performance for photocatalytic process, since photo generated charge carrier can rapidly move to the surface of the catalysts, or redox

organic molecule. For example, bismuth sulfide (Bi_2S_3) nanomaterials were used as a photocatalyst to degrade congo red dye, and the reaction process occurs under UV light conditions [27,30]. Bi_2S_3 additionally belongs to the category of nontoxic semiconductor materials. Moreover, semiconducting materials for optoelectronics shows high absorption coefficient (104 cm^{-1}) range [31]. This material is a proper photocatalytic behavior for the enhancement of electron movement.

In this present work, the single source precursor [Bi(DTC)] have been used for preparation of Bi_2S_3 NPs and HDA as capping and shape directing agent by solvothermal method. As-prepared Bi_2S_3 NPs have been successfully examined with electrochemical super capacitive behaviour for energy storage application. In addition, the Bi_2S_3 NPs have been utilized for the effective photocatalytic discoloration of the CR dye in aqueous medium under UV light irradiation. Moreover stability and reusability also studied.

2. Experimental part

2.1 Materials and Methods

Bismuth (III) nitrate [$Bi(NO_3)_3.5H_2O$], Sodium diethyldithiocarbamate [$C_5H_{10}NNaS_2.3H_2O$], N, N-Dimethylformamide (DMF) [C_3H_7NO], And potassium hydroxide [KOH], Hexadecylamine (HDA) [$C_{16}H_{35}N$] and ethanol [C_2H_5OH], methanol [CH_3OH] all chemical were received from Sigma Aldrich Pvt. Ltd with AR Grade. Congo red textile dye was purchased from local market with commercial grade. The metal complex synthesis was performed in DI water.

2.2 Preparation of Bi[DTC] (Single source Precursor) Complex

In typical preparation, equal molar ratio of bismuth (III) Nitrate (4.85g) and Sodium Diethyldithiocarbamate [Na(DTC)] (4.50g) was separately dissolved with 100 ml of deionized

(DI) water with 1 h continuously stirred and mixed together with drop by drop. The yellowish green colour precipitation was formed. Then, it was allowed to continuous stirring for 2h. after, homogeneous mixing the yellow colour precipitate has been separated and washed several time by DI water and ethanol by centrifugal force. The resulting material was continuously desiccated at 60 °C for 12 h. After cooling to the room temperature Bi[DTC] complex were collected for further use [16].

2.3 Preparation of Bismuth sulfide (Bi_2S_3) NPs from Bi[DTC] complex

The prepared Bi[DTC] complex as precursor and Hexadecylamine (HAD) as capping agent and shape directing agent were utilized in 1:1 weight ratio and dispersed in 100 ml of N, N-Dimethylformamide (DMF). Then the above mixture is heated at 120 °C for 1h by solvothermal method. Finally, dark colour precipitate was collected and washed with Methanol for remove un-reactant. The final product (Bi_2S_3 NPs) was collected and dried in oven at 60 °C for overnight and used to confirm with different analytical methods are shown in **Fig. 1.**

Figure 1.

2.4 Instrumentation

Crystalline nature of the prepared Bi_2S_3 NPs was examined by Powder X-ray diffractometer using Bruker instrument of model D8 advance ECO XRD frameworks with SSD160 1D Detector which has Cu-Kα radiation of frequency 1.5406 Å. The Surface morphological were studied by scanning electron microscope instrument ZEISS EVO 18 which was outfitted with BRUKER X-Flash 6130 equipped with energy dispersive X-beam spectrometer to confirm the elements of Bi_2S_3 NPs. An instrument Shimadzu IR Trace-100 spectrometer was utilized to record the

infrared range of arranged unadulterated Bi_2S_3 test by KBr pellet approach. The Raman ridiculous investigation was recorded on laser Raman Microscope (Raman-11,500 mm spectrometer Nano photon Corporation Japan). Higher Resolution Transmission Electron Microscope (HR-TEM) was utilized to trace the structural morphologies of the prepared sample.

2.5 Working electrode preparation

The electrochemical reaction of the Bi_2S_3 electrodes was investigated in 1M KOH electrolyte by utilizing three electrodes system electrochemical work station CHI6008E. The electrode material of Bi_2S_3 was organized utilizing 0.01mm thick and $1cm^2$ Nickel foil for electrochemical execution investigation. At first, the outside of Ni foil was wind-swept with emery sheet and took into consideration sonication, at that point cleaned with $(CH_3)_2CO$. Bi_2S_3 material, Activated carbon, polyvinylidene fluoride (PVDF) cover was blended in with the weight proportion of 80:10:10 and ground well for blending homogeneous blend. What's more, a drop of N-methyl-2-pyrrolidone (NMP) was added to the blend to make it as slurry and afterward it was applied as, a slight film on nickel foil. It was dried at 80 °C during 12hrs further the electrode was used to analysis of electrochemical studies.

2.6 Photocatalytic Experiments

The photodegradation experiment was performed using Bi_2S_3 NPs as active catalyst for the effective photo discoloration commercial Congo Red dye under UV-light (λ=365 nm) irradiation. The experiment was studied by with help of HEBER Photo reactor (Model – HML–MP 88). 50 mg of Bi_2S_3 NPs was used as catalyst in aqueous medium. CR dye was used of 5×10^{-5} M of concentration. Every 15 min. 1.5 ml of reaction solution was reserved for monitor the

absorption value of CR dye was used for degradation. A control experiment was performed without catalyst for CR dye degradation.

3. Results and Discussion

3.1 X-ray Diffraction analysis

The XRD analysis for the as-prepared Bi_2S_3 NPs showed in fig 2. The indexed diffraction peaks are noticed at 2θ values 15.61, 17.54, 22.35, 23.51, 24.85, 28.51, 31.6, 35.45, 39.68, 45.27, 46.42, 48.93, 52.4, 58.94, 62.41, 64.72, 69.34, 71.85 and 84.75 correspond to hkl value (0 2 0), (1 2 0), (2 2 0), (1 0 1), (1 3 0), (2 3 0), (2 2 1), (2 4 0), (1 4 1), (0 0 2), (4 3 1), (0 2 2), (1 3 2), (4 6 0), (4 3 2), (5 6 0), (1 6 2), (5 4 2), and (4 7 2) respectively, The positions and comparative intensities of the considerable number of peaks are in acceptable understanding, with those are orthorhombic crystalline formation for Bi_2S_3 NPs and they are indexed to standard JCPDS card number 89-8964. The all around coordinates with the average cell parameters morals (a = 11.13 Å, b = 11.29 Å, and c = 3.981 Å). The standard grain sizes are determined from the expansion of the X-Ray diffraction peaks utilizing the Scherrer method.

$$D = 0.9\lambda / \beta\cos\theta \qquad \text{..... (1)}$$

Where, D - standard grain size, λ - X-ray wavelength (0.15405nm) and θ and β - diffraction angle as well as full-width at half maximum in radians of the experimentally observed peak correspondingly [9, 21]. The average grain sizes of prepared Bi_2S_3 NPs were ~54.7 nm.

Figure 2

3.2 FTIR spectrum

Fig.3 shows the FT-IR spectra of as-prepared Bi_2S_3 nanoparticles were recorded to confirmed the prepared nanoparticles via its vibration and their intermolecular interactions. In Fig.3, a small weak vibration peak appeared around 554 cm^{-1} due to rocking vibration of bismuth metal [32]. The broad peaks found in the range of 1300 to 1370 cm^{-1} due to interaction between sulfur-atmospheric carbon and oxygen bonding. In the range of 2842 to 2913 cm^{-1} observed two bands of N–H and OH stretching vibration [33–35]. Apart from these no other peaks were found in FTIR spectrum it clearly evident for free from impurities.

Figure 3

3.3 Raman spectrum

Raman spectroscopy is an effective inorganic tool to identify materials in structural approach [36]. Therefore, the Bi_2S_3 NPs were recorded Raman spectrum at room temperature in the range of 0 to 2000 cm^{-1} was shown in Fig.4. The spectrum has four distinct vibrational peaks of approximately 260,306, 420, and 967 cm^{-1} the order coincides with the Bi_2S_3 characteristics peaks, which are stable with the previously reported significance in the research. A strong peak occurred at an altitude of 967cm^{-1} due to the high surface to volume ratio of surface phonon modes [37,38].

Figure 4

3.4 Thermal stability of Bi[DTC] metal complex

Fig.5 shows the TG-DTA curve of the Bismuth diethyldithiocarbamate Bi[DTC] complex, the complex was tested under Nitrogen atmosphere. From the thermo gravimetric graph some miles

weight occurred due to solvent evaporation and second weight loss starting from 119.7 °C onwards due to decomposition of unreacted Sodium Dithiocarbamate. In the range of 192 °C starts a major weight loss due to Bi[DTC] complex at the point the metal complex fully converted in to metal sulfides Bi_2S_3 up to 41.8 % weight loss shows in this region due to single source precursor converted in metal sulfides in this region further after heating the heat exchange from 195 to 317.3 °C, this might be because of the evaporation of the sulfur. The final decomposition stage about 3.7% at the temperature range 503.5°C and No weight loss about above 503.5 °C. This could be additionally distinguished by the observable three endothermic top about 149 °C, 283.7 °C, and 479.5 °C respectively in the DTA curves. Apart from this curve no weight loss were found the remaining residue is confirmed as Metal sulfides (Bi_2S_3).

Figure 5

3.5 SEM and EDAX with mapping analysis

Surface morphological analysis and shape of the as-prepared Bi_2S_3 nanoparticles were examined by SEM images as shown in Fig.6. From the morphological studies uniform rod-spherical shaped Bi_2S_3 NPs were found in Fig.6 (a, b). It is clearly shows the HDA capped Bi_2S_3 NPs uniformly distributed throughout the sample. The purity of synthesized Bismuth sulfide nanoparticles is declared since the energy dispersive X-ray spectrum. The appeared Fig.7 (a) an energy dispersive X-ray spectrum along with Fig.7 (b) uncovers mapping images of synthesized Bismuth sulfide (Bi_2S_3) nanoparticles. The inset showed in Fig. 7 (a) as the mass level of Bi and S is resolute by EDAX (energy dispersive X-ray) analysis. An EDAX study shows that the all around cleaned the last thing is commonly made out of Bismuth (Bi) and Sulfur (S), through cannot be present any extra unwanted components Fig.7 (a). It has the in accumulation the

average atomic gain of Sulfur (S) was especially elevated from the energy dispersive X-ray image 59.5 % and Bismuth (Bi) peak contained in the range of 40.5 %.

Figure 6

Figure 7

3.6 HR-TEM analysis

The structural and morphology of the prepared Bi_2S_3 nanoparticles were characterized by high resolution transmission electron microscope. Fig. 8 (a-d) shows the nanostructured Bi_2S_3 Nanoparticles with mixed morphologies like nanoplates and spherical in shaped NPs and this shows, more number of spherical shape nanoparticles were aggregate and to form rod shape structure Fig. 8 (a, b). The average size of the nanoparticles observed around ~20 nm thickness to micro meter range. This result coincides with SEM and XRD analysis. Hexadecylamine did the vital role for capping and shape directing agent. The atomic lattice fringes are clearly observed in an HR-TEM micrograph and a d-spacing value of 0.540 nm range were shown in Fig.8 (c). Fig.8 (d) displays the selected area electron diffraction (SAED) pattern of the Bi_2S_3 nanoparticles. From the SAED pattern clearly shows concentrical diffraction rings of orthorhombic crystalline structure and Bi_2S_3 nanoparticles verified the polycrystalline nature preferably distinct single crystal.

Figure 8

3.7 XPS analysis

The surface chemical oxidation state and binding energy of the spherical shaped Bi_2S_3 NPs were probed by XPS studies, from this result (Fig. 9). Fig 10 (a) no impurities peaks were observed in the full survey trace excluding Bi, S, O and C. The atomic sensitivity factor of Bismuth and

sulfur ratio is around 2:3 according to quantification of the Bi4f and S2s peak surface area, signifying the stoichiometric composition of Bi_2S_3 and this result coincided with EDX studies. The two higher resolution spectra of $Bi4f_{7/2}$ and $Bi4f_{5/2}$ spin orbit doublet are traced at 157.8 and 163.1 eV respectively [39]. The small peak appeared at 161.5 eV for S2p owing to the primary valance state of sulfur[40]. The Fig. 10(b) shows the strong peak found at 228.2 eV corresponding to the binding energy (B.E) of S2s [41]. The C1s peak is found at 284.5 eV and all spectra are corrected with carbon spectrum as a reference is shown in Fig. 10 (c). The oxygen element may present due to adsorption or contamination of atmosphere on the Bi_2S_3 surface (Fig. 10(d)).

Figure 9

Figure 10

3.8 Cyclic Voltammetry analysis

The electrochemical performances of the Bi_2S_3 modified electrode material have been evaluate by the Cyclic Voltammetry (CV) results. The above mentioned method was using to analyse by three-electrode system with 1 M KOH as electrolyte solution. Fig.11 (a) shows that The Cyclic Voltammetry curves of the Bi_2S_3 electrode material was studied at various scan rates (1 - 100 mVs^{-1}) in the potential windows ranging from 0 to 0.6 (V) Vs (Ag/AgCl). The CV curves revealed high oxidation and reduction peaks have been present in the potential range at 0.52 (V) and 0.33 (V) respectively. The redox behavior of CV results directly exhibit pseudo capacitive nature of the electrode material. The redox equation of the Bi_2S_3 electrode material becomes

$$Bi_2S_3 + OH^- \leftrightarrow Bi_2S_3 + H_2O + e^- \quad \text{..... (2)}$$

Furthermore, the redox peaks shift to negative or positive due to increments of scan rates, which exhibit the internal diffusion resistance in the electrode material[42].

The Randles-Sevcik plot was shown in the fig. 11(b) after the completion of CV test. It was explain the linear increase of specific peak current for anode and cathode side (i.e., Redox) with respect to the square root of scan rate. From the Randles graph, value of R_2 was seen at 0.97405 for anodic (oxidation) and 0.97091 for cathodic (reduction) process respectively. This exact parameter was because of the limited diffusion process of static reversible faradaic reaction [43,44].

The specific capacitance value of the Bi_2S_3 NPs working electrodes has been calculated from the CV curves and GCD curves by using the formulas (3) and (4)

$$C_{sp}\ (Fg^{-1}) = \frac{\int Idv}{mv\ \Delta V} \qquad \text{..... (3)}$$

Where, ∫Idv (A) is the integral area under the Cyclic Voltammetry curves, v is the scan rate (mV s^{-1}), m (g) is the mass of active electrode material, and ΔV (V) is the potential difference

$$C_{sp}\ (Fg^{-1}) = \frac{I \times \Delta t}{\Delta V \times m} \qquad \text{..... (4)}$$

Where, m (g) is the mass of the active electrode material, ΔV (V) is the potential difference, Δt (s) is the discharge time, and I (A) is the constant discharge current**.**

The calculated specific capacitance values of scan rates 1-100 mVs^{-1} were shown in Fig.11 (c). The individual values of specific capacitance and different scan rates are given in table 1. At minimum scan rate 1 mVs^{-1}, active electrode surface area is high for involving in electrochemical reaction. The increasing scan rates to restrict the electrolyte ions towards moving to the electrode active site, which reflects the decreasing specific capacitance[45].

Figure 11

Table 1

3.9 Chronopotentiometry

Galvanostatic charging discharge (or) chronopotentiometry was analysis the different current density range (0.5 to 10 A g^{-1}) of Bi_2S_3 electrode material. Fig.12 (a) shows charge discharge curve it was indicates the ability of the Bi_2S_3 electrode. On the basis, the specific capacitances increase with due to increase discharging time. The charge/discharge curve was interpreted as due to this redox reactions occure interface between the electrode and electrolyte. The higher current densities have higher internal resistance drop, its closely relative to the charge transfer resistance [46].

Fig.12 (b) explains the variation between specific capacitance and current density of Bi_2S_3 electrode material. The equation 4 is to calculate the value of specific capacitance from current density. The calculate value of specific capacitance of Bi_2S_3 electrode with various current density was shown in table 2. In addition, increasing specific capacitance was obtained at lower current density. Correspondingly, the surface interfaces and higher inside activates accessible charge/discharge at lower current densities. Form this study, Bi_2S_3 electrode material conclude that for 0.5 A g^{-1} current density and high specific capacitance be 470 F g^{-1}, this C_{sp} value is higher than as previous report, S. Vadivel (290 F g^{-1}) [17], K.L. Liu (233 F g^{-1}) [47], K. Liang (270 F g^{-1}) [48] and A.K Noordeen (152.2 F g^{-1}) [49], S.S Raut (289 F g^{-1}) [50] L. Ma (185.7 Fcm^{-2}) [51], respectively. Table 3, shows the comparison of specific capacitance for the same electrode materials with various preparation methods.

The electrochemical impedance spectrum of Bi_2S_3 was studied in the 1Hz to 1MHz. The impedance performance of Bi_2S_3 was shown before and after 1000 cycles in the fig.12 (c). The corresponding Niquiest plot was fitted with Z view software. The Niquiest plot consist three regions namely low, high and mid frequency regions. In addition, the phase angle as a function of frequency is mentioned as a Bode plot was shown in the fig.12 (d). This reveals the solution resistance and charge transfer resistance of the Bi_2S_3 NPs. it was evalued value of phase angle near to -70° in frequency frame of impedance study shows the perfect capacitive behavior Bi_2S_3 electrode material [52].

The impedance parameter was mentioning the table 4. The solution resistance of the Bi_2S_3 becomes 0.89 Ω and charge transfer resistance have 1.96 Ω. The absorption of OH- ions enhanced to flux vacancy of the cations from the metal electrolyte toward metal sulfide surfaces. The interfaces metal exchanged cations[53]. The equivalent circuit was shown in the fig.12 (c). The high frequency region semicircle reveals the sluggish redox reaction kinetics, charge transfer resistance of the Bi_2S_3 electrode its become 1.96 Ω. The Warburg regions exhibit the diffusion of the electrode material due to ions in the electrolyte. Obviously, the low frequency region slope shows the fast absorption of the ion mobility in the electrolyte on the surface of the electrode[54].

The Ragone plot of Bi_2S_3 electrode was calculated from the three electrode analysis[46]. The power density and energy density figure was shown in fig.12 (e) Bi_2S_3 of the electrode materials. The Bi_2S_3 electrode material shows a higher energy density 16.31 Wh kg^{-1} (with power density 125 Wkg^{-1}) and power density of 2500 Wkg^{-1} (with energy density 8.3 Wh kg^{-1}. In the term, the acquired value of energy density is beyond that previous reported like Bi_2S_3:PbS (13.36 Wh kg^{-1}), [55] and Co_3So_4 (27.77 Wh kg^{-1}) [56]. The cycle performance and electrode stability

was analyzed from the charge discharge method up to 1000 cycles in fig.12 (f). The cycle test was linearly decreasing, its exhibit stability of the electrode material. Finally Bi_2S_3 test holds for 79 % of original value of the capacitance. The impedance spectrum of Bi_2S_3 was after 1000 cycle exhibit the electrode stability in the electrolyte. This represents the best cathodic electrode material for supercapacitor devices.

Figure 12

Table 2

Table 3

Table 4

3.10 Photodegradation Studies

In order to study photocatalytic activities for the prepared Bi_2S_3 nanoparticles was utilized against commercial Congo Red (CR) textile dye under UV-Vis. light irradiation. At first 50 mg of Bi_2S_3 catalyst was loaded in100 ml of 1×10^{-5} M of CR dye aqueous solution [57]. A control reaction was carried out under dark room condition for 15 minutes with photocatalyst to attain equilibrium condition between CR dye and Bi_2S_3 nanocatalyst with exposed λ=365 nm UV-light irradiation continuously up to 150 munities. 3 ml of reaction solution was withdrawn with every 15 min. to monitor the absorbance intensity of CR dye at 498 and 364 nm using UV-Vis. Spectrometer. Finally, the nano catalyst were collected using centrifuge machine and washed with DI water followed by methanol and dried at 70 °C for 4 h to reuse the catalyst. The same procedure will followed by further consecutive testing.

The Fig. 13(A) shows the UV- Vis. Absorption spectra of CR at 50 mg of Bi_2S_3 NPs loaded on 100 ml of aqueous dye. The spectra shows visibly and gradually reduced the CR dye

intensity with respect of UV exposed time. The same experiment was carried out without catalyst named as blank with similar irradiation time. From the UV absorbance spectra was obviously conclude the role of catalyst on CR dye medium. Fig. 13(B) shows the concentration (C/C_0) plot of CR with and without catalyst. In the case of bank (without catalyst) the colour was not change after 150 min. UV irradiation and it is periodically monitored with UV-Spectrometer after removal of Bi_2S_3 catalyst. In-opposite periodically CR dye intensity was reduced in presence of as prepared and Calcinated Bi_2S_3 samples as shown in Fig. 13(B). The CR dye exhibits two major peaks in the region of 364 and 498 nm respective to the naphthalene (aromatic) rings and $\pi-\pi*$ transitions of (-N=N-) azo group. The aqueous CR solution $\lambda_{(Max)}$ = 498 nm gradually suppressed under UV light irradiation in the presence of Bi_2S_3 catalyst. In the case of 364 nm gradually decrease with slight shifting towards lower wavelength. It May indicate that azo bonds are more vulnerable to degradation than the aromatic rings by hydroxyl radicals [58]. Hence it is proved the single source precursor fabricated spherical shaped Bi_2S_3 NPs have excellent photocatalytic performance under UV light irradiation.

The degradation efficiency can calculate by the equation (3),

$$\eta = C_0 - C/C_0 \times 100 \quad \text{..... (5)}$$

Where, 'C_0' is initial concentration of dye and 'C' is the concentration after irradiation time (t). More over the calibration linear plot are fitted with Irradiation time and $\ln(C/C_0)$ and compared as shown in Fig. 13(C). The degradation rate constant (k) were calculated from slop of linear fit line, according to first order kinetic act $\ln(C/C_0)=kt$ [59,60]. The R^2 value and rate constant (K) of Bi_2S_3 NPs was found R^2=0.99 and k= 0.0127. The results of rate constant and linear regression coefficient (R^2) suggest that the Bi_2S_3 sample revealed superior photo catalytic performance. Possible mechanism of photodegradation are given below,

$Bi_2S_3 + h\upsilon \rightarrow Bi_2S_3\,(e^- + h^+)$ …….. (6)

$e^- + O_2 \rightarrow O_2^{\cdot -}$ ……. (7)

$h^+ + H_2O \rightarrow OH^{\cdot} + H^+$ ……. (8)

$O_2^{\cdot -}$ /$OH^{\cdot}$ + (CR) dye →(CR) $dye_{(redox)}$ (benzene + naphthalene derivatives) ……. (9)

OH**.** + benzene/naphthalene derivatives → $CO_2 + H_2O$. …… (10)

The Bi_2S_3 NPs was exposed under UV light irradiation which resulted in the electrons (e^-) excitation from valance band to conduct band while leaving holes (h^+) in the valance band. The e^- and generated O_2 are formed as radical and h^+ in the valance band were absorbed the water molecule then produced $OH^{\cdot}$, H^+ radical which is lead to facilitate to degrade the CR dye molecules as shows in the above equations.

3.11 Catalyst stability and Reusability studies

The stability and reusability of the prepared catalyst are very important in catalysis application. Because it can reduce the overall expenditure for the waste water treatment. In this connection, the prepared Bi_2S_3 NPs were examined used as catalyst among five successive cycles of photodegradation were carried out using the same catalyst other than fresh solution of CR dye in aqueous medium. After each reuse the catalyst was washed with methanol and dried at 80 °C for 3h. The % of degradation was 97.3, 94.8, 92.4, 90.6 and 86.4 for 1 to 5^{th} cycles respectively. It was noticed that good and constant decrement of the photocatalyst efficiency up to 4^{th} cycle and after 4^{th} cycle an immediate drop will occurred as shown in Fig. 13(D). Hence it is concluded, the spherical shaped nanoparticles were highly stable up to 4 cycles. These experimental results suggested that, the Bi_2S_3NPs have excellent stability and reusability and practically applicable to degrade environmental water contamination.

Figure 13

4. Conclusions

Bi_2S_3 NPs has been successfully accomplished by using solvothermal method. The synthesized Bi_2S_3 nanoparticle was characterized for XRD plot indicated that the crystalline nature was orthorhombic crystalline structure. Raman and FT-IR spectral studies have clarify the presence of functional group in the synthesized nanomaterials. Furthermore, we in addition inspected, the morphology of Bi_2S_3 nanoparticle was capture by SEM result of identical, nanoparticle-like morphology with a spherical shape. Photocatalytic discoloration of CR dye was investigated using Bi_2S_3 NPs under UV and visible light irradiation. The sample was fully degraded among 150 min of irradiation in presence of UV-visible light, and the restriction for the stability of photocatalytic degradation were superior. The Bi_2S_3 NPs was water purify steady up to 5^{th} cycles it will be utilized to degrade the CR dye degradation under UV-Vis. light. In addition, The Bi_2S_3 NPs electrode material was exhibits high specific capacitance at 470 Fg^{-1} and current density value at 0.5 Ag^{-1}. Likewise, they performed great cyclic stability of 79 % at after 1000 cycles. Finally the prepared Bi_2S_3 NPs material was perfect energy storage and photocatalytic applications.

Acknowledgements

Author C. S and P. D have thankfully acknowledged Kalasalingam Academy of Research and Education (KARE) for given University Research Fellowship (URF) and providing research facilities.

Reference

[1] A. Moyseowicz, Scalable one-pot synthesis of bismuth sulfide nanorods as an electrode active material for energy storage applications, J. Solid State Electrochem. 23 (2019) 1191–1199. https://doi.org/10.1007/s10008-019-04215-7.

[2] A. Moyseowicz, G. Gryglewicz, Hydrothermal-assisted synthesis of a porous polyaniline/reduced graphene oxide composite as a high-performance electrode material for supercapacitors, Compos. Part B Eng. 159 (2019) 4–12. https://doi.org/https://doi.org/10.1016/j.compositesb.2018.09.069.

[3] Z. Wu, Y. Sun, Y. Tan, S. Yang, X. Feng, K. Müllen, Three-Dimensional Graphene-Based Macro- and Mesoporous Frameworks for High-Performance Electrochemical Capacitive Energy Storage, J. Am. Chem. Soc. 134 (2012) 19532–19535. https://doi.org/10.1021/ja308676h.

[4] S. Yang, X. Feng, L. Wang, K. Tang, J. Maier, K. Müllen, Graphene-Based Nanosheets with a Sandwich Structure, Angew. Chemie Int. Ed. 49 (2010) 4795–4799. https://doi.org/doi:10.1002/anie.201001634.

[5] A. Śliwak, N. Díez, E. Miniach, G. Gryglewicz, Nitrogen-containing chitosan-based carbon as an electrode material for high-performance supercapacitors, J. Appl. Electrochem. 46 (2016) 667–677. https://doi.org/10.1007/s10800-016-0955-z.

[6] M.P. Motaung, J. Osuntokun, D.C. Onwudiwe, The heat-up synthesis of monodispersed Bi_2S_3 and Cu_7S_4 nanoparticles from novel precursor complexes and their characterizations, Mater. Sci. Semicond. Process. 99 (2019) 92–98. https://doi.org/10.1016/j.mssp.2019.04.024.

[7] B. Weng, M. Qi, C. Han, Z. Tang, Y. Xu, Photocorrosion Inhibition of Semiconductor-

Based Photocatalysts : Basic Principle , Current Development , and Future Perspective, ACS Catal. 9 (2019) 4642–4687. https://doi.org/10.1021/acscatal.9b00313.

[8] D.C. Onwudiwe, P.A. Ajibade, ZnS, CdS and HgS Nanoparticles via Alkyl-Phenyl Dithiocarbamate Complexes as Single Source Precursors, Int. J. Mol. Sci. 12 (2011) 5538–5551. https://doi.org/10.3390/ijms12095538.

[9] J. Arumugam, A.D. Raj, A.A. Irudayaraj, Reaction time dependent investigation on the properties of the Bi_2S_3 nanoparticles: Photocatalytic application, Mater. Today Proc. 5 (2018) 16094–16099. https://doi.org/https://doi.org/10.1016/j.matpr.2018.05.092.

[10] S.V.P. Vattikuti, A.K.R. Police, J. Shim, C. Byon, Sacrificial-template-free synthesis of core-shell C@Bi_2S_3 heterostructures for efficient supercapacitor and H2 production applications, Sci. Rep. 8 (2018) 4194. https://doi.org/10.1038/s41598-018-22622-0.

[11] X. Chen, Q. Wang, L. Wang, F. Gao, W. Wang, Z. Hu, Imidazoline derivative templated synthesis of broccoli-like Bi_2S_3 and its electrocatalysis towards the direct electrochemistry of hemoglobin, Biosens. Bioelectron. 66 (2015) 216–223. https://doi.org/https://doi.org/10.1016/j.bios.2014.11.020.

[12] A. Singh, A.J. Roberts, R.C.T. Slade, A. Chandra, High electrochemical performance in asymmetric supercapacitors using MWCNT/nickel sulfide composite and graphene nanoplatelets as electrodes, J. Mater. Chem. A. 2 (2014) 16723–16730. https://doi.org/10.1039/C4TA02870H.

[13] F. Amirian, M. Molaei, M. Karimipour, A.R. Bahador, A new and simple UV-assisted approach for synthesis of water soluble ZnS and transition metals doped ZnS nanoparticles (NPs) and investigating optical and photocatalyst properties, J. Lumin. 196 (2018) 174–180. https://doi.org/10.1016/j.jlumin.2017.12.005.

[14] P. Devendran, T. Alagesan, K. Pandian, Single pot microwave synthesis of CdS nanoparticles in ionic liquid and their photocatalytic application, in: Asian J. Chem., 2013.

[15] H. Rao, W. Sun, S. Ye, W. Yan, Y. Li, H. Peng, Z. Liu, Z. Bian, C. Huang, Solution-Processed CuS NPs as an Inorganic Hole-Selective Contact Material for Inverted Planar Perovskite Solar Cells, ACS Appl. Mater. Interfaces. 8 (2016) 7800–7805. https://doi.org/10.1021/acsami.5b12776.

[16] P. Devendran, T. Alagesan, A. Manikandan, S. Asath Bahadur, M. Krishna Kumar, S. Rathinavel, K. Pandian, Sonochemical Synthesis of Bi_2S_3 Nanowires Using Single Source Precursor and Their Electrochemical Activity, Nanosci. Nanotechnol. Lett. 8 (2016) 478–483. https://doi.org/10.1166/nnl.2016.2111.

[17] S. Vadivel, A.N. Naveen, V.P. Kamalakannan, P. Cao, N. Balasubramanian, Facile large scale synthesis of Bi_2S_3 nano rods–graphene composite for photocatalytic photoelectrochemical and supercapacitor application, Appl. Surf. Sci. 351 (2015) 635–645. https://doi.org/10.1016/j.apsusc.2015.04.101.

[18] M.D. Regulacio, M.-Y. Han, Composition-Tunable Alloyed Semiconductor Nanocrystals, Acc. Chem. Res. 43 (2010) 621–630. https://doi.org/10.1021/ar900242r.

[19] X. Xin, M. He, W. Han, J. Jung, Z. Lin, Low-Cost Copper Zinc Tin Sulfide Counter Electrodes for High-Efficiency Dye-Sensitized Solar Cells, Angew. Chemie Int. Ed. 50 (2011) 11739–11742. https://doi.org/doi:10.1002/anie.201104786.

[20] H. Zhong, Z. Bai, B. Zou, Tuning the Luminescence Properties of Colloidal I–III–VI Semiconductor Nanocrystals for Optoelectronics and Biotechnology Applications, J. Phys. Chem. Lett. 3 (2012) 3167–3175. https://doi.org/10.1021/jz301345x.

[21] E. Sathiyaraj, S. Thirumaran, Structural, morphological and optical properties of iron

sulfide, cobalt sulfide, copper sulfide, zinc sulfide and copper-iron sulfide nanoparticles synthesized from single source precursors, Chem. Phys. Lett. 739 (2020) 136972. https://doi.org/10.1016/j.cplett.2019.136972.

[22] H. Zhou, S. Xiong, L. Wei, B. Xi, Y. Zhu, Y. Qian, Acetylacetone-Directed Controllable Synthesis of Bi_2S_3 Nanostructures with Tunable Morphology, Cryst. Growth Des. 9 (2009) 3862–3867. https://doi.org/10.1021/cg801405e.

[23] P.K. Panigrahi, A. Pathak, The Growth of Bismuth Sulfide Nanorods from Spherical-Shaped Amorphous Precursor Particles under Hydrothermal Condition, J. Nanoparticles. 2013 (2013) 1–11. https://doi.org/10.1155/2013/367812.

[24] A. Begum, A. Hussain, A. Rahman, Optical and Electrical Properties of Doped and Undoped Bi_2S_3-PVA Films Prepared by Chemical Drop Method, Mater. Sci. Appl. 02 (2011) 163–168. https://doi.org/10.4236/msa.2011.23020.

[25] R. Chen, M.H. So, C.-M. Che, H. Sun, Controlled synthesis of high crystalline bismuth sulfide nanorods: using bismuth citrate as a precursor, J. Mater. Chem. 15 (2005) 4540–4545. https://doi.org/10.1039/B510299E.

[26] J. Chao, S. Xing, J. Zhao, C. Qin, D. Duan, Y. Zhao, Q. He, Bismuth sulfide nanoflowers as high performance near-infrared laser detectors and visible-light-driven photocatalysts, RSC Adv. 6 (2016) 55676–55681. https://doi.org/10.1039/C6RA06339J.

[27] Z. Fang, Y. Liu, Y. Fan, Y. Ni, X. Wei, K. Tang, J. Shen, Y. Chen, Epitaxial Growth of CdS Nanoparticle on Bi_2S_3 Nanowire and Photocatalytic Application of the Heterostructure, The. 115Journal (2011) 13968–13976. https://doi.org/10.1021/jp112259p.

[28] P. Devendran, T. Alagesan, N. Nallamuthu, S. Asath Bahadur, K. Pandian, Single-

precursor synthesis of sub-10 nm CdS nanoparticles embedded on graphene sheets nanocatalyst for active photodegradation under visible light, Appl. Surf. Sci. 534 (2020) 147614. https://doi.org/10.1016/j.apsusc.2020.147614.

[29] Q. Hao, C. Xie, Y. Huang, D. Chen, Y. Liu, W. Wei, B.-J. Ni, Accelerated separation of photogenerated charge carriers and enhanced photocatalytic performance of g-C_3N_4 by Bi_2S_3 nanoparticles, Chinese J. Catal. 41 (2020) 249–258. https://doi.org/https://doi.org/10.1016/S1872-2067(19)63450-9.

[30] G. ZHAO, Y. ZHENG, Z. HE, Z. LU, L. WANG, C. LI, F. JIAO, C. DENG, Synthesis of Bi_2S_3 microsphere and its efficient photocatalytic activity under visible-light irradiation, Trans. Nonferrous Met. Soc. China. 28 (2018) 2002–2010. https://doi.org/https://doi.org/10.1016/S1003-6326(18)64844-7.

[31] B. Li, Y. Zhang, R. Du, L. Gan, X. Yu, Synthesis of Bi_2S_3–Au Dumbbell Heteronanostructures with Enhanced Photocatalytic and Photoresponse Properties, Langmuir. 32 (2016) 11639–11645. https://doi.org/10.1021/acs.langmuir.6b03213.

[32] J. Arumugam, A. Dhayal Raj, A. Albert Irudayaraj, Solvent effects on the properties of Bi_2S_3 nanoparticles: photocatalytic application, J. Mater. Sci. Mater. Electron. 28 (2017) 3487–3494. https://doi.org/10.1007/s10854-016-5947-6.

[33] S. Ranjitha, S. Vadivel, J. Marimuthu, S. Natarajan, Structural and Optical Properties of Bismuth Sulfide Nanoparticles, (2014) 20–21.

[34] M. Salavati-Niasari, Z. Behfard, O. Amiri, Synthesis of bismuth sulfide nanostructures by using bismuth(III) monosalicylate precursor and fabrication of bismuth sulfide based p–n junction solar cells, Asia-Pacific J. Chem. Eng. 9 (2014) 16–23. https://doi.org/doi:10.1002/apj.1741.

[35] P. Nazari, R. Dowlatabadi-Bazaz, M.R. Mofid, M.R. Pourmand, N.E. Daryani, M.A. Faramarzi, Z. Sepehrizadeh, A.R. Shahverdi, The Antimicrobial Effects and Metabolomic Footprinting of Carboxyl-Capped Bismuth Nanoparticles Against Helicobacter pylori, Appl. Biochem. Biotechnol. 172 (2014) 570–579. https://doi.org/10.1007/s12010-013-0571-x.

[36] J. Ota, S.K. Srivastava, Polypyrrole Coating of Tartaric Acid-Assisted Synthesized Bi_2S_3 Nanorods, J. Phys. Chem. C. 111 (2007) 12260–12264. https://doi.org/10.1021/jp072906y.

[37] S. Sharma, N. Khare, Hierarchical Bi_2S_3 nanoflowers : A novel photocatalyst for enhanced photocatalytic degradation of binary mixture of Rhodamine B and Methylene blue dyes and degradation of mixture of ... Hierarchical Bi_2S_3 nanoflowers : A novel photocatalyst for enhance, Adv. Powder Technol. (2018). https://doi.org/10.1016/j.apt.2018.09.012.

[38] S.R. Kadam, R.P. Panmand, R.S. Sonawane, S.W. Gosavi, B.B. Kale, A stable Bi_2S_3 quantum dot–glass nanosystem: size tuneable photocatalytic hydrogen production under solar light, RSC Adv. 5 (2015) 58485–58490. https://doi.org/10.1039/C5RA10244H.

[39] S. Wang, W. Li, H. Song, C. Mao, Z. Zhang, H. Peng, G. Li, Nitrogen-enriched carbon-coated flower-like bismuth sulfide architectures towards high-performance lithium-ion battery anodes, Inorg. Chem. Front. 6 (2019) 1275–1281. https://doi.org/10.1039/c9qi00062c.

[40] H.-P. Jiao, X. Yu, Z.-Q. Liu, P.-Y. Kuang, Y.-M. Zhang, One-pot synthesis of heterostructured Bi_2S_3/BiOBr microspheres with highly efficient visible light photocatalytic performance, RSC Adv. 5 (2015) 16239–16249. https://doi.org/10.1039/C4RA16948D.

[41] A. Moyseowicz, Scalable one-pot synthesis of bismuth sulfide nanorods as an electrode active material for energy storage applications, J. Solid State Electrochem. 23 (2019) 1191–1199. https://doi.org/10.1007/s10008-019-04215-7.

[42] X. Zhai, J. Gao, X. Xu, W. Hong, H. Wang, F. Wu, Y. Liu, 3D interconnected Bi_2S_3 nanosheets network directly grown on nickel foam as advanced performance binder-free electrode for hybrid asymmetric supercapacitor, J. Power Sources. 396 (2018) 648–658. https://doi.org/10.1016/j.jpowsour.2018.06.081.

[43] B. Chameh, M. Moradi, S. Kaveian, Synthesis of hybrid ZIF-derived binary ZnS/CoS composite as high areal-capacitance supercapacitor, Synth. Met. 260 (2020) 116262. https://doi.org/10.1016/j.synthmet.2019.116262.

[44] S. Ezhil Arasi, P. Devendran, R. Ranjithkumar, S. Arunpandiyan, A. Arivarasan, Electrochemical property analysis of zinc vanadate nanostructure for efficient supercapacitors, Mater. Sci. Semicond. Process. 106 (2020) 104785. https://doi.org/https://doi.org/10.1016/j.mssp.2019.104785.

[45] B. Pandit, G.K. Sharma, B.R. Sankapal, Chemically deposited Bi_2S_3:PbS solid solution thin film as supercapacitive electrode, J. Colloid Interface Sci. 505 (2017) 1011–1017. https://doi.org/10.1016/j.jcis.2017.06.092.

[46] S.J. Patil, J.H. Kim, D.W. Lee, Graphene-nanosheet wrapped cobalt sulphide as a binder free hybrid electrode for asymmetric solid-state supercapacitor, J. Power Sources. 342 (2017) 652–665. https://doi.org/10.1016/j.jpowsour.2016.12.096.

[47] K.L. Liu, F. Chen, Y. Liu, D. Li, W.D. Shi, Synthesis of hierarchical Bi_2S_3 nanoflowers via a topotactic transformation from hierarchical Bi_2WO_6 nanoflowers and their supercapacitor performance, CrystEngComm. 19 (2017) 570–575.

https://doi.org/10.1039/C6CE02410F.

[48] K. Liang, C. Wang, X. Xu, J. Leng, H. Ma, Capacitive and photocatalytic performance of Bi_2S_3 nanostructures synthesized by solvothermal method, Phys. Lett. A. 381 (2017) 652–657. https://doi.org/https://doi.org/10.1016/j.physleta.2016.12.005.

[49] A.K. Noordeen, S. Sambasivam, S. Chinnasamy, J. Ramasamy, T. Subramani, Hierarchical Flower Structured Bi_2S_3/Reduced Graphene Oxide Nanocomposite for High Electrochemical Performance, J. Inorg. Organomet. Polym. Mater. 28 (2018) 73–83. https://doi.org/10.1007/s10904-017-0701-y.

[50] S.S. Raut, J.A. Dhobale, B.R. Sankapal, SILAR deposited Bi_2S_3 thin film towards electrochemical supercapacitor, Phys. E Low-Dimensional Syst. Nanostructures. 87 (2017) 209–212. https://doi.org/10.1016/j.physe.2016.09.019.

[51] L. Ma, Q. Zhao, Q. Zhang, M. Ding, J. Huang, X. Liu, Y. Liu, X. Wu, X. Xu, Controlled assembly of Bi_2S_3 architectures as Schottky diode, supercapacitor electrodes and highly efficient photocatalysts, RSC Adv. 4 (2014) 41636–41641. https://doi.org/10.1039/C4RA07169G.

[52] B. Pandit, G.K. Sharma, B.R. Sankapal, Chemically deposited Bi_2S_3:PbS solid solution thin film as supercapacitive electrode, J. Colloid Interface Sci. 505 (2017) 1011–1017. https://doi.org/https://doi.org/10.1016/j.jcis.2017.06.092.

[53] Z. Grubać, M. Metikoš-Huković, EIS study of solid-state transformations in the passivation process of bismuth in sulfide solution, J. Electroanal. Chem. 565 (2004) 85–94. https://doi.org/10.1016/j.jelechem.2003.09.036.

[54] E. Miniach, G. Gryglewicz, Solvent-controlled morphology of bismuth sulfide for supercapacitor applications, J. Mater. Sci. 53 (2018) 16511–16523.

https://doi.org/10.1007/s10853-018-2785-3.

[55] B. Pandit, S.A. Pande, B.R. Sankapal, Facile SILAR Processed Bi_2S_3:PbS Solid Solution on MWCNTs for High-performance Electrochemical Supercapacitor, Chinese J. Chem. 37 (2019) 1279–1286. https://doi.org/10.1002/cjoc.201900222.

[56] S.J. Patil, J.H. Kim, D.W. Lee, Graphene-nanosheet wrapped cobalt sulphide as a binder free hybrid electrode for asymmetric solid-state supercapacitor, J. Power Sources. 342 (2017) 652–665. https://doi.org/10.1016/j.jpowsour.2016.12.096.

[57] P. Devendran, T. Alagesan, T.R. Ravindran, K. Pandian, Synthesis of Spherical CdS Quantum Dots Using Cadmium Diethyldithiocarbamate as Single Source Precursor in Olive Oil Medium, Curr. Nanosci. 10 (2014) 302–307. https://doi.org/10.2174/15734137113096660117.

[58] D. Malwal, P. Gopinath, Enhanced photocatalytic activity of hierarchical three dimensional metal oxide@CuO nanostructures towards the degradation of Congo red dye under solar radiation, Catal. Sci. Technol. 6 (2016) 4458–4472. https://doi.org/10.1039/c6cy00128a.

[59] K. Ravichandran, R. Mohan, B. Sakthivel, S. Varadharajaperumal, P. Devendran, T. Alagesan, K. Pandian, Enhancing the photocatalytic efficiency of sprayed ZnO thin films through double doping (Sn + F) and annealing under different ambiences, Appl. Surf. Sci. 321 (2014) 310–317. https://doi.org/10.1016/j.apsusc.2014.10.023.

[60] M. Thiruppathi, P. Senthil Kumar, P. Devendran, C. Ramalingan, M. Swaminathan, E.R. Nagarajan, Ce@TiO_2 nanocomposites: An efficient, stable and affordable photocatalyst for the photodegradation of diclofenac sodium, J. Alloys Compd. 735 (2018) 728–734. https://doi.org/10.1016/j.jallcom.2017.11.139.

Figure Captions

Fig. 1. Schematic representation for the Bi_2S_3 nanoparticles synthesis

Fig. 2. Powder XRD spectrum of as-prepared Bi_2S_3 nanoparticles

Fig. 3. Representative FTIR spectrum of as-prepared Bi_2S_3 NPs

Fig. 4. Raman spectrum of as-synthesized Bi_2S_3 nanoparticles

Fig. 5. Thermo gravimetric analysis of the Bi[DTC] complex

Fig. 6 SEM image of synthesized Bi_2S_3 NPs at 200 nm range

Fig. 7. (a) EDS spectrum of Bi_2S_3 NPs and (b) mapping images of prepared Bi_2S_3 NPs

Fig. 8 (a-c) HR-TEM analysis with different magnifications and (d) SEAD pattern of Bi_2S_3 NPs

Fig. 9. X-ray Photoelectron Spectroscopy full survey spectrum of spherical shaped Bi_2S_3 NPs

Fig. 10. XPS higher resolution spectra of (a) Bi4f (b) $S2_S$ (c) $C1_S$ (d) $O1_S$

Fig. 11. (a) CV curves at different scan rates, (b) Oxidation peak current (Ia) and reduction peak current (Ic) various scan rates, and (c) Specific capacitance vs scan rate

Fig. 12. (a) galvanostatic charge-discharge curves at different current densities, (b) Specific capacitance vs current density, (c) EIS spectra, (d) Bode plot for before and after 1000 cycles, (e) Ragone plot related to power densities and energy densities of Bi_2S_3 NPs, (f) Specific capacitance variation over 1000 charge-discharge cycles at 5 A g^{-1}, and retentivity plot of Bi_2S_3 NPs

Fig. 13. (A) Photocatalytic degradation of Congo Red (CR) dye using Bi_2S_3 as photocatalyst,

(B) Degradation profiles of CR in the presence of Bi_2S_3 NPs and hierarchical nanostructures

(C) Photodegradation calibration plot, (D) recycle efficiency of the photocatalyst, photocatalytic efficiency of the reused Bi_2S_3 NPs for the degradation of CR dye

Figures

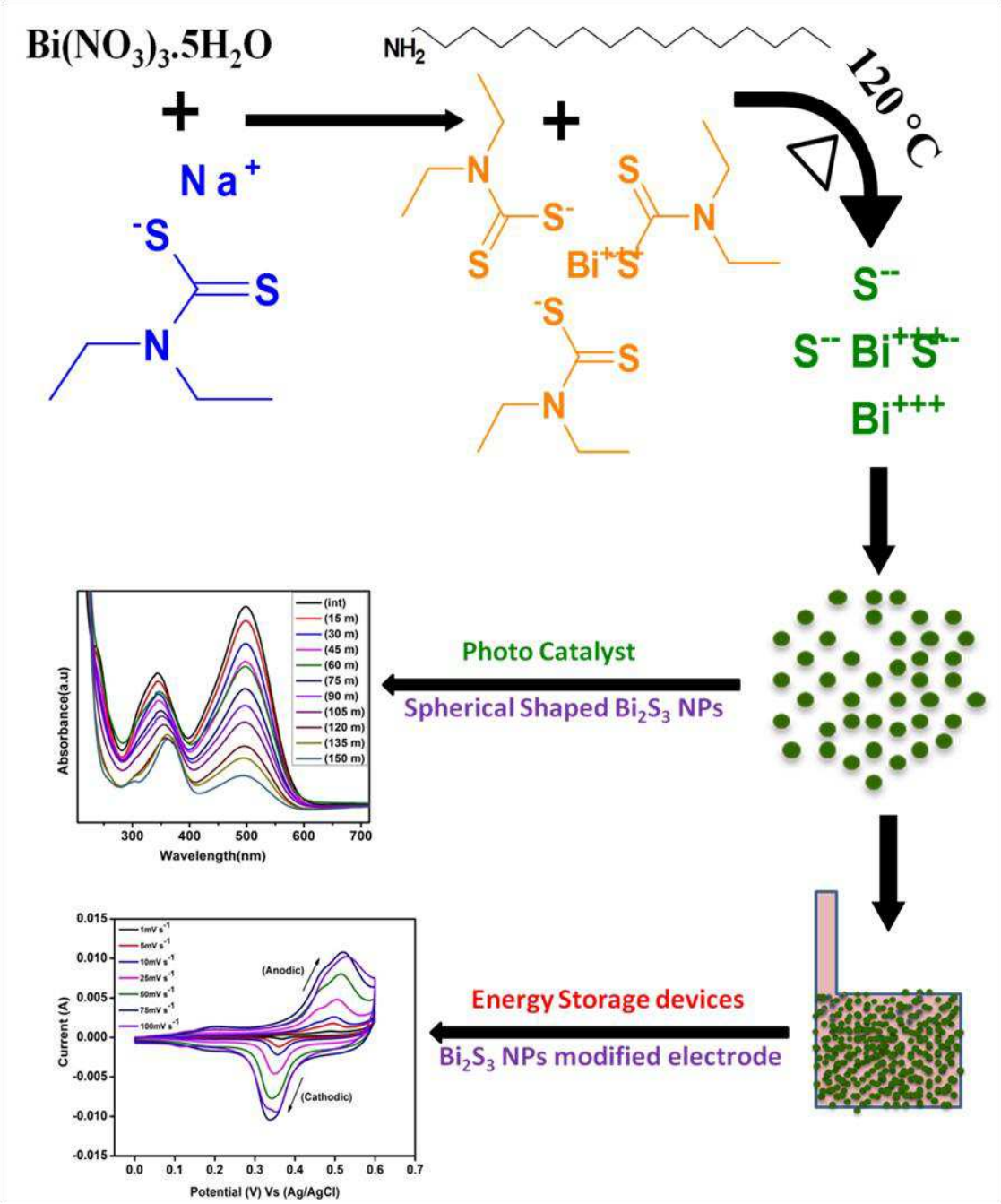

Fig. 1

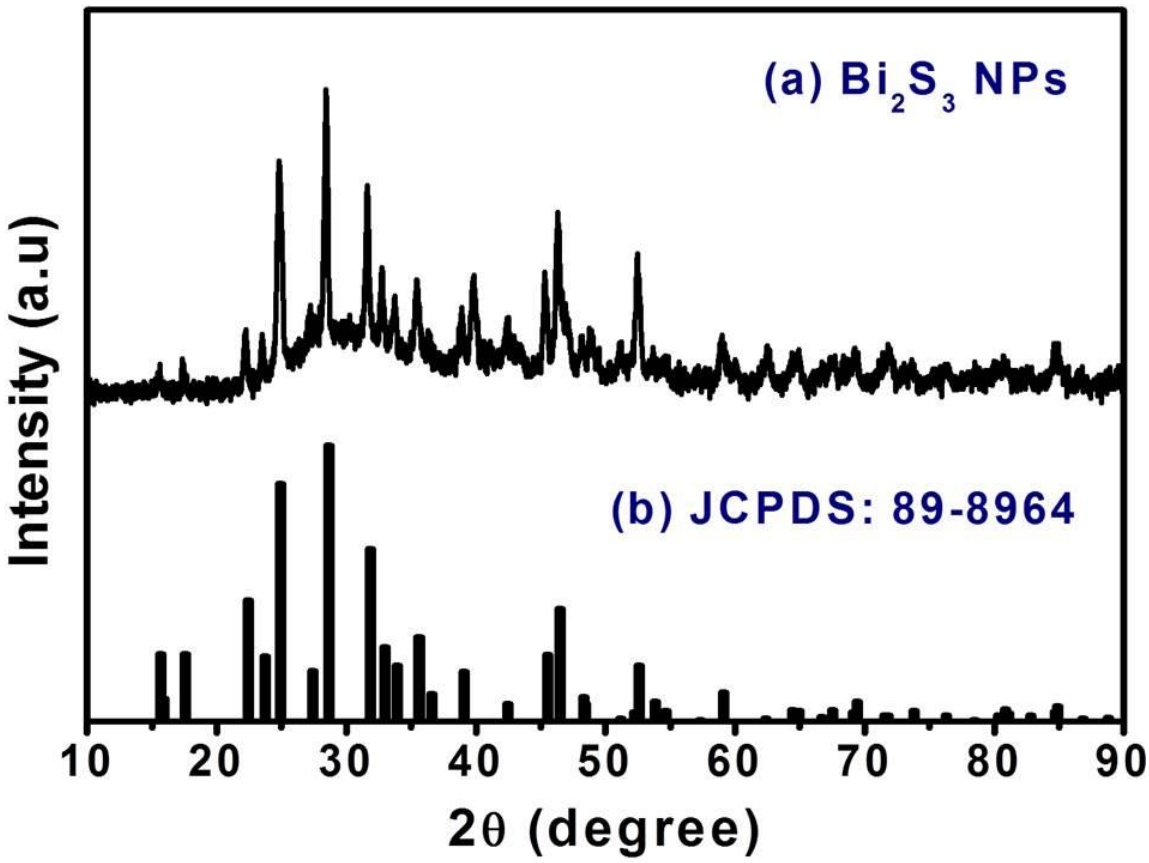
(a) Bi_2S_3 NPs
(b) JCPDS: 89-8964
Intensity (a.u)
10
20
30
40
50
60
70
80
90
2θ (degree)

Fig. 2

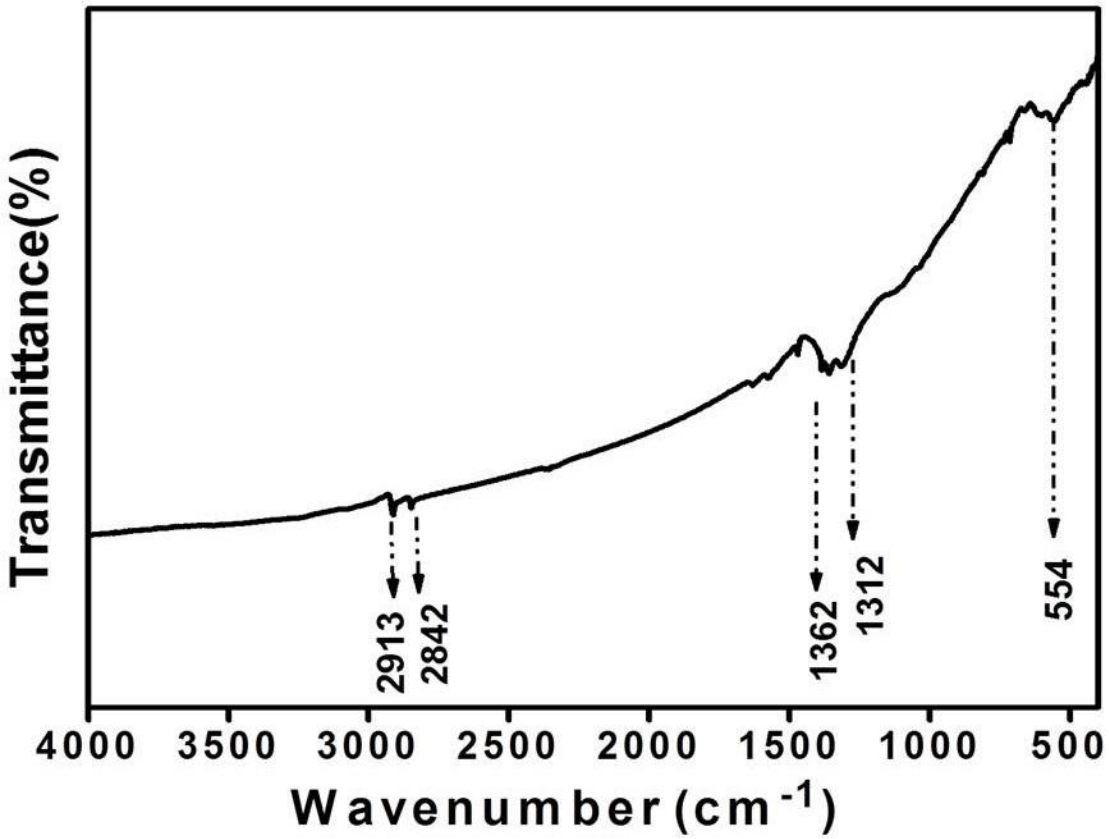
Transmittance(%)
2913
2842
1362
1312
554
4000
3500
3000
2500
2000
1500
1000
500
Wavenumber (cm-1)

Fig. 3.

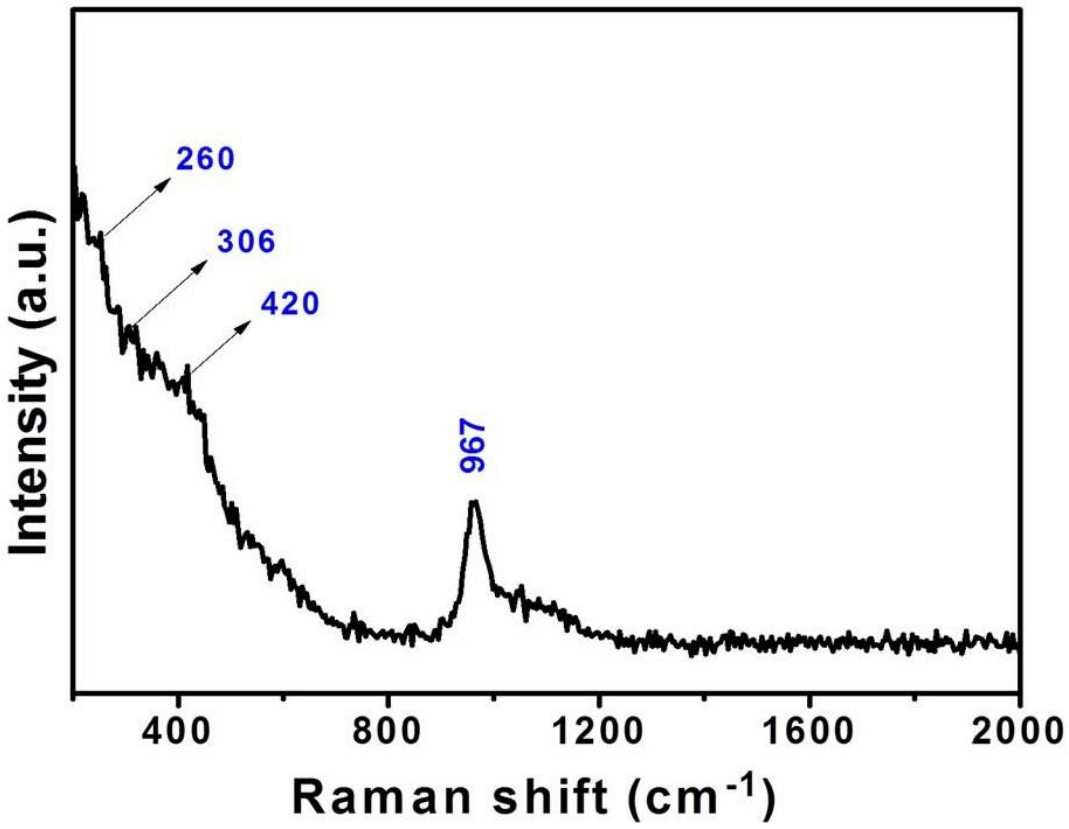
260
306
420
967
Intensity (a.u.)
400
800
1200
1600
2000
Raman shift (cm-1)

Fig. 4

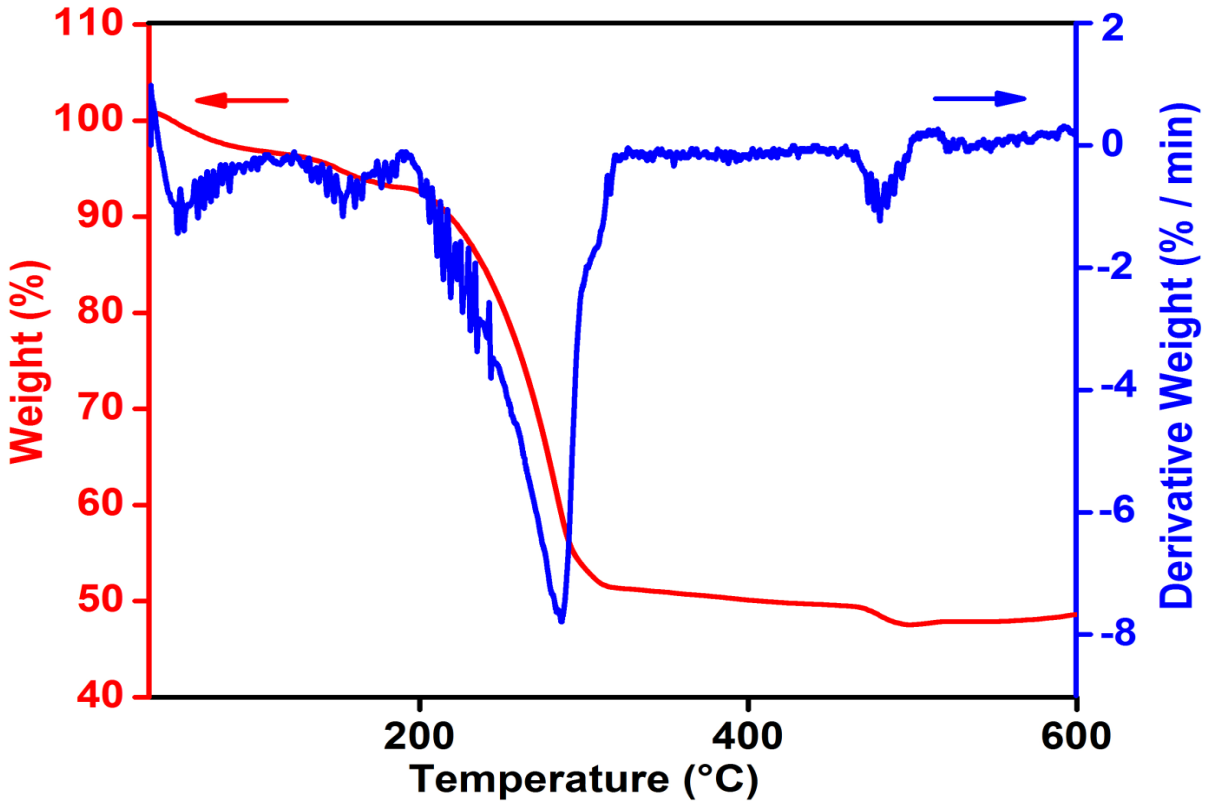
110
100
90
80
70
60
50
40
Weight (%)
200
400
600
Temperature (°C)
2
0
-2
-4
-6
-8
Derivative Weight (% / min)

Fig. 5

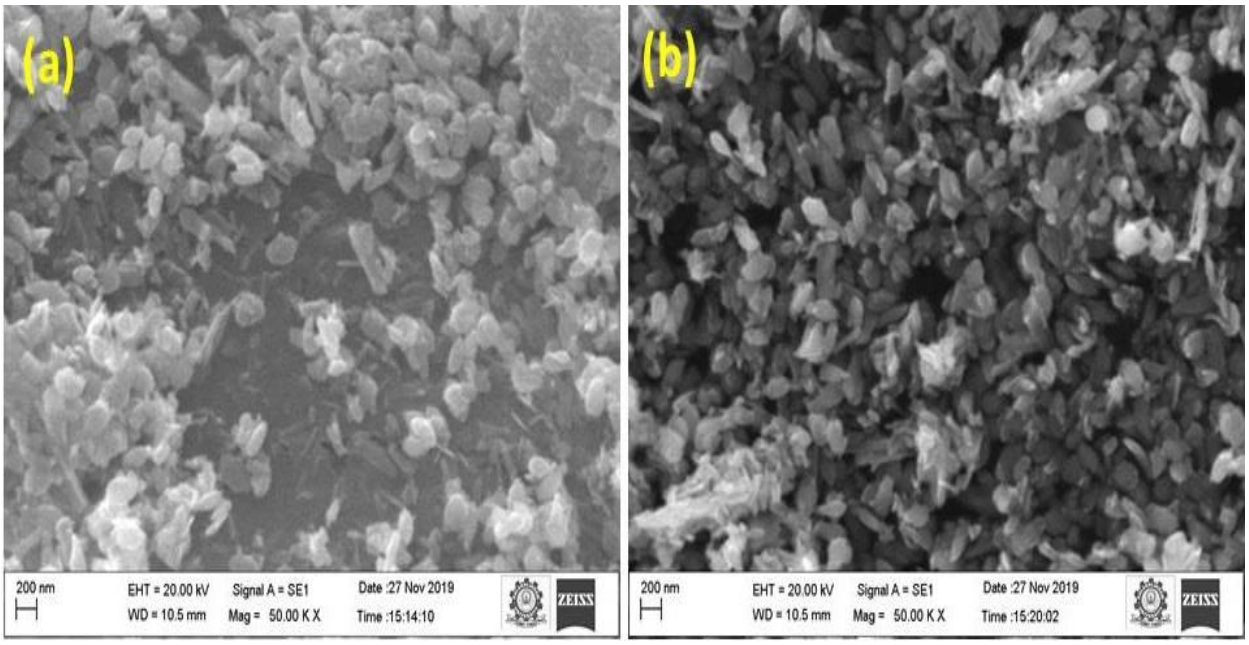
(a)
200 nm
EHT = 20.00 kV
WD = 10.5 mm
Signal A = SE1
Mag = 50.00 K X
Date :27 Nov 2019
Time :15:14:10
ZEISS
(b)
200 nm
EHT = 20.00 kV
WD = 10.5 mm
Signal A = SE1
Mag = 50.00 K X
Date :27 Nov 2019
Time :15:20:02
ZEISS

Fig. 6

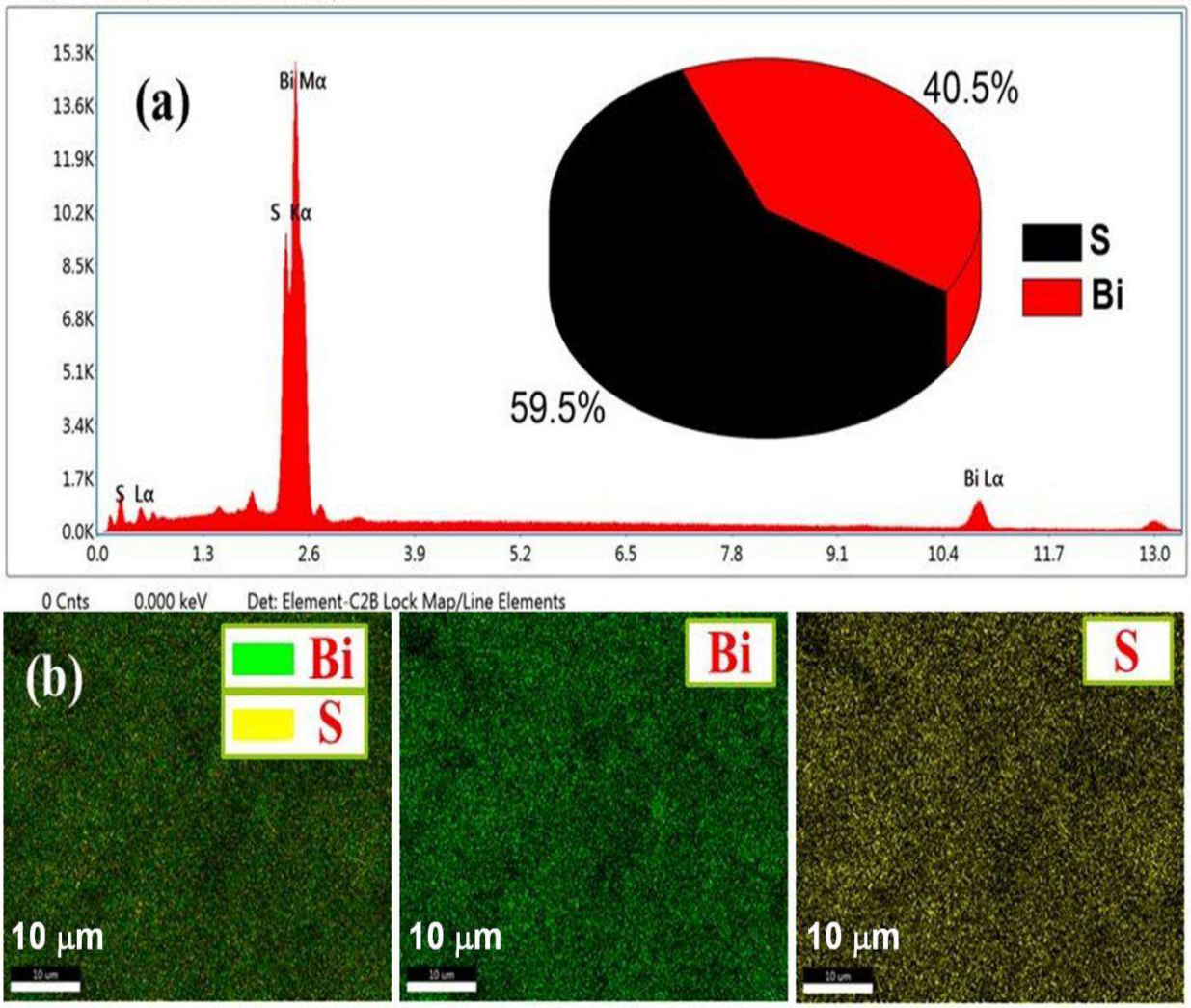
(a)
Bi Mα
S Kα
S Lα
Bi Lα
40.5%
59.5%
S
Bi
15.3K
13.6K
11.9K
10.2K
8.5K
6.8K
5.1K
3.4K
1.7K
0.0K
0.0
1.3
2.6
3.9
5.2
6.5
7.8
9.1
10.4
11.7
13.0
0 Cnts
0.000 keV
Det: Element-C2B Lock Map/Line Elements
(b)
Bi
S
10 μm
Bi
10 μm
S
10 μm

Fig. 7

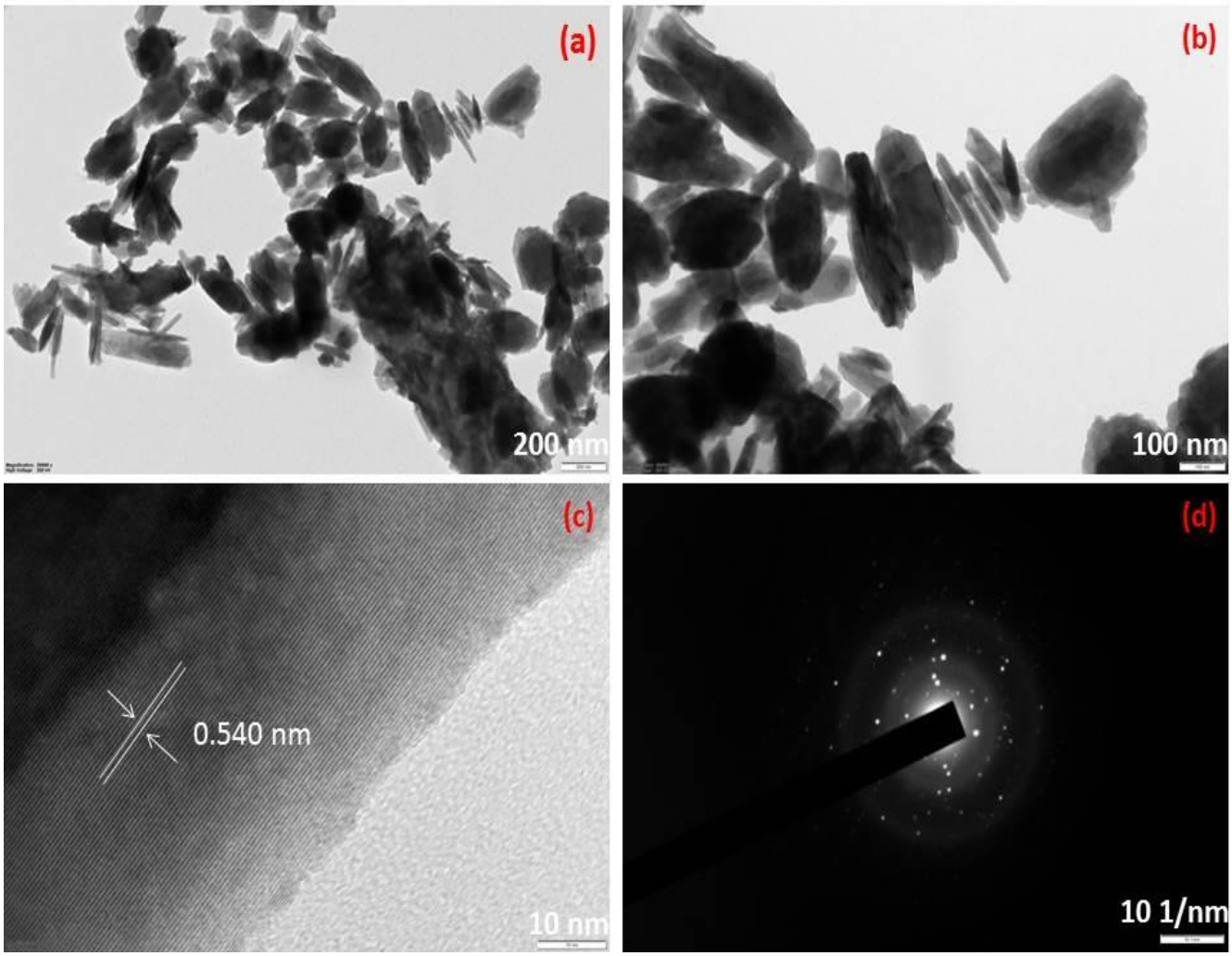

Fig. 8

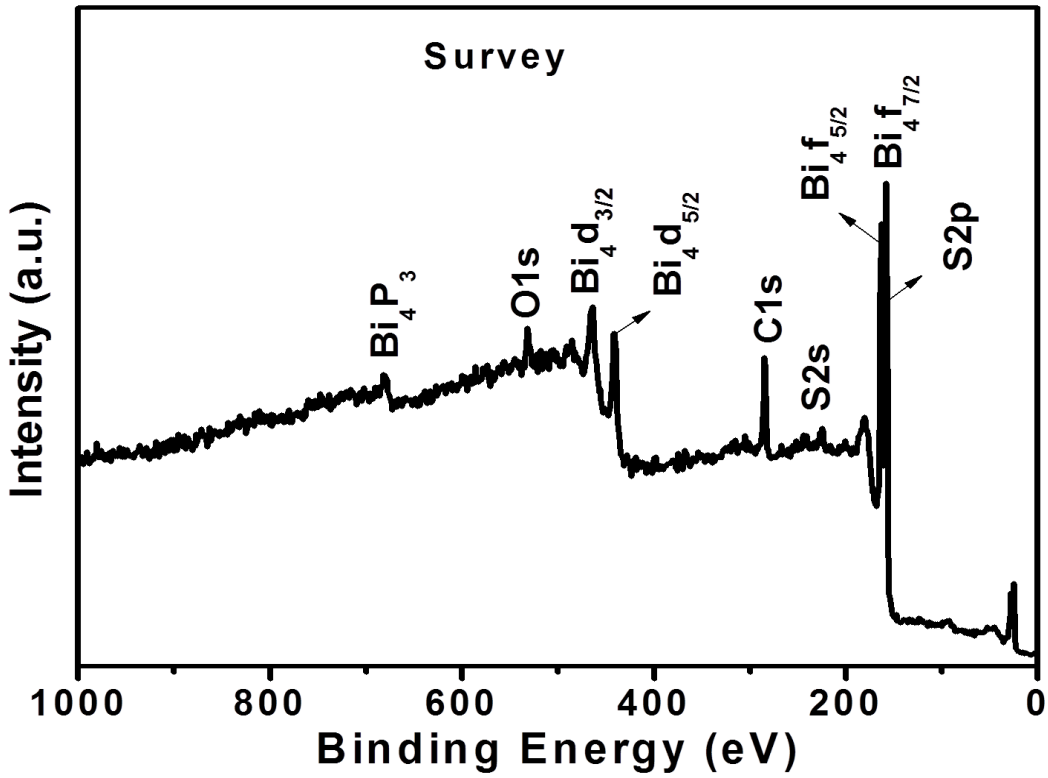
Survey
Intensity (a.u.)
Bi 4P 3
O1s
Bi 4d 3/2
Bi 4d 5/2
C1s
S2s
Bi 4f 5/2
Bi 4f 7/2
S2p
1000
800
600
400
200
0
Binding Energy (eV)

Fig. 9

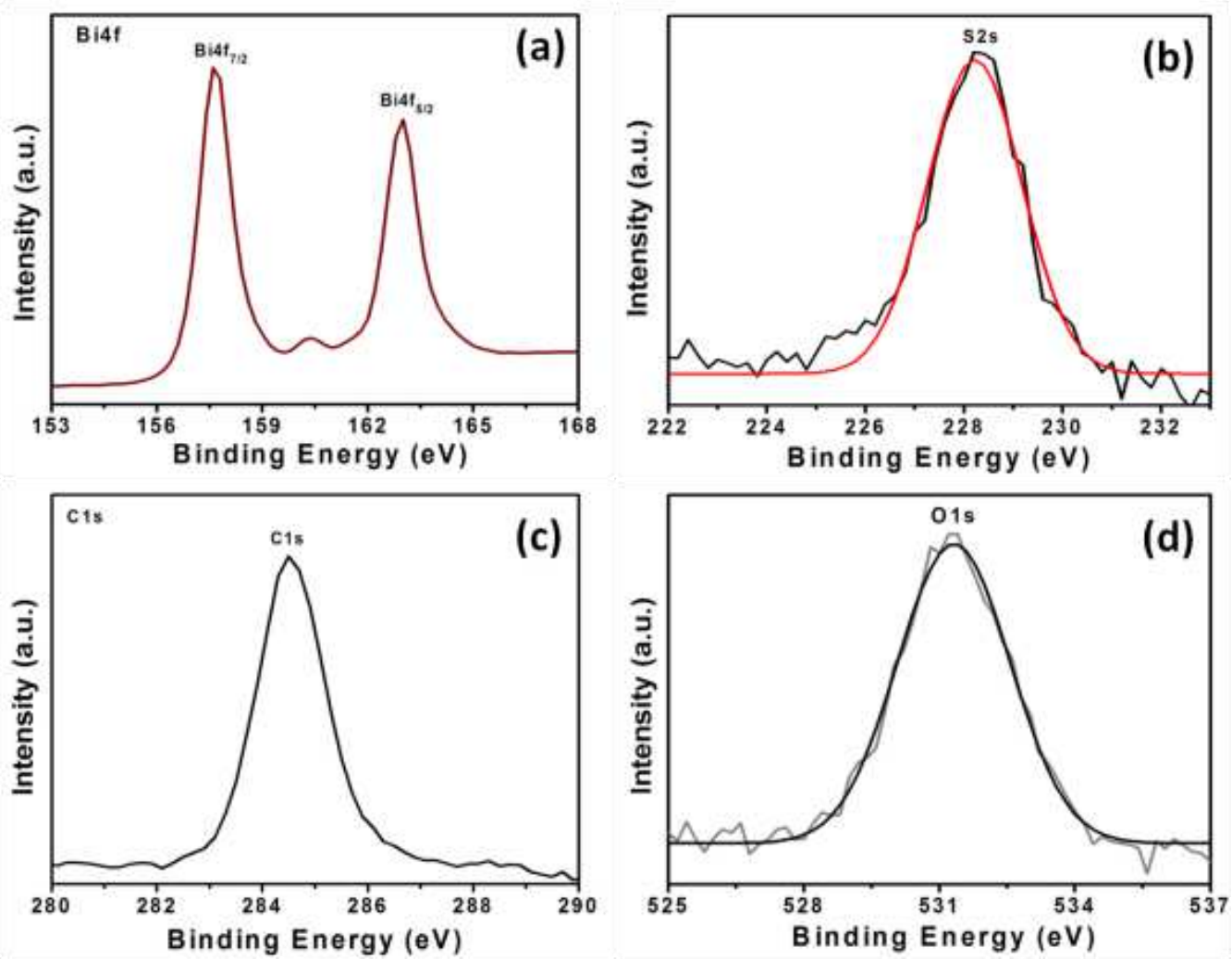
Bi4f
Bi4f7/2
Bi4f5/2
(a)
Intensity (a.u.)
153
156
159
162
165
168
Binding Energy (eV)
S2s
(b)
Intensity (a.u.)
222
224
226
228
230
232
Binding Energy (eV)
C1s
C1s
(c)
Intensity (a.u.)
280
282
284
286
288
290
Binding Energy (eV)
O1s
(d)
Intensity (a.u.)
525
528
531
534
537
Binding Energy (eV)

Fig. 10

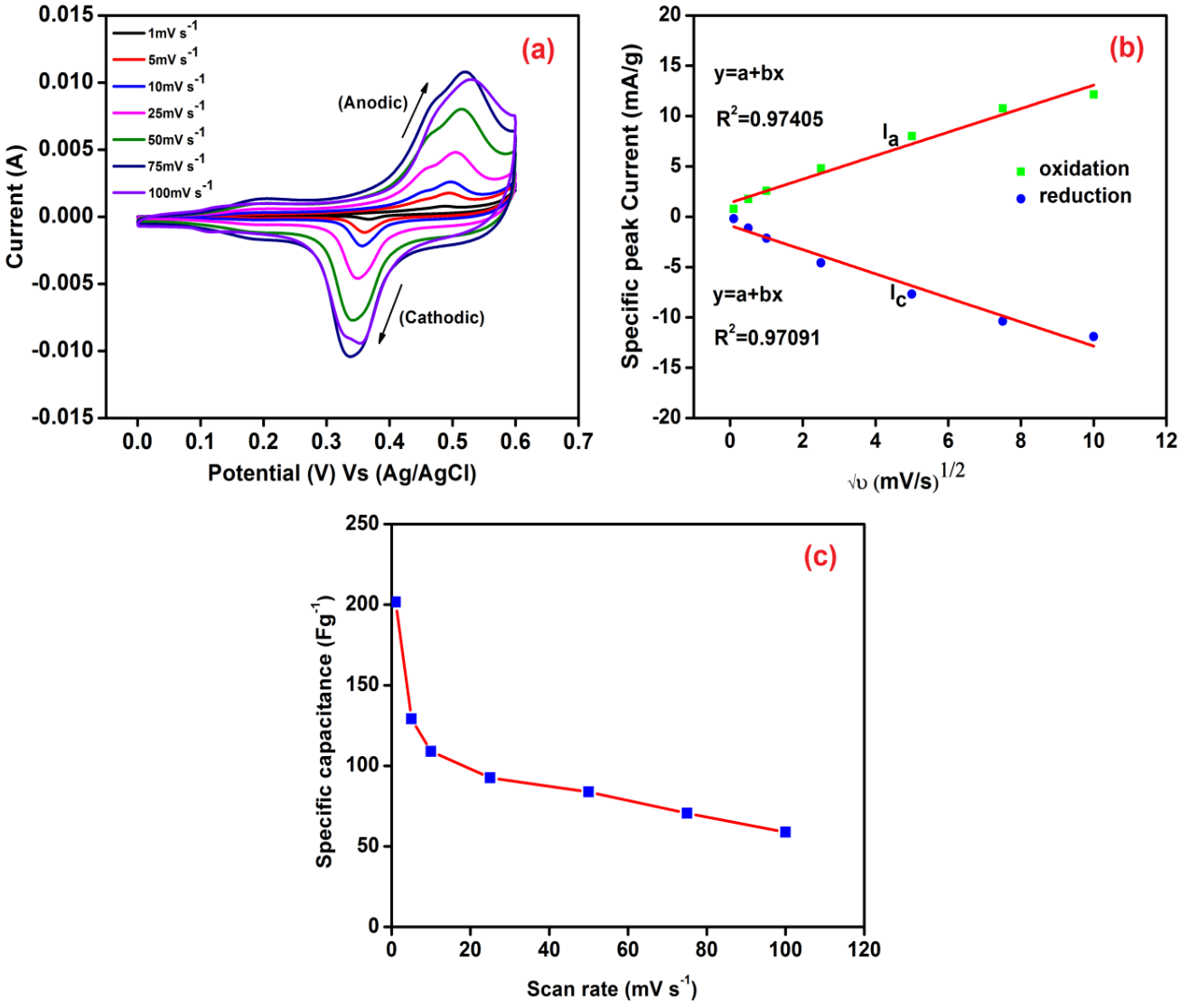
(a)
1mV s-1
5mV s-1
10mV s-1
25mV s-1
50mV s-1
75mV s-1
100mV s-1
(Anodic)
(Cathodic)
Current (A)
Potential (V) Vs (Ag/AgCl)
(b)
y=a+bx
R2=0.97405
Ia
oxidation
reduction
y=a+bx
R2=0.97091
Ic
Specific peak Current (mA/g)
√υ (mV/s)1/2
(c)
Specific capacitance (Fg-1)
Scan rate (mV s-1)

Fig. 11

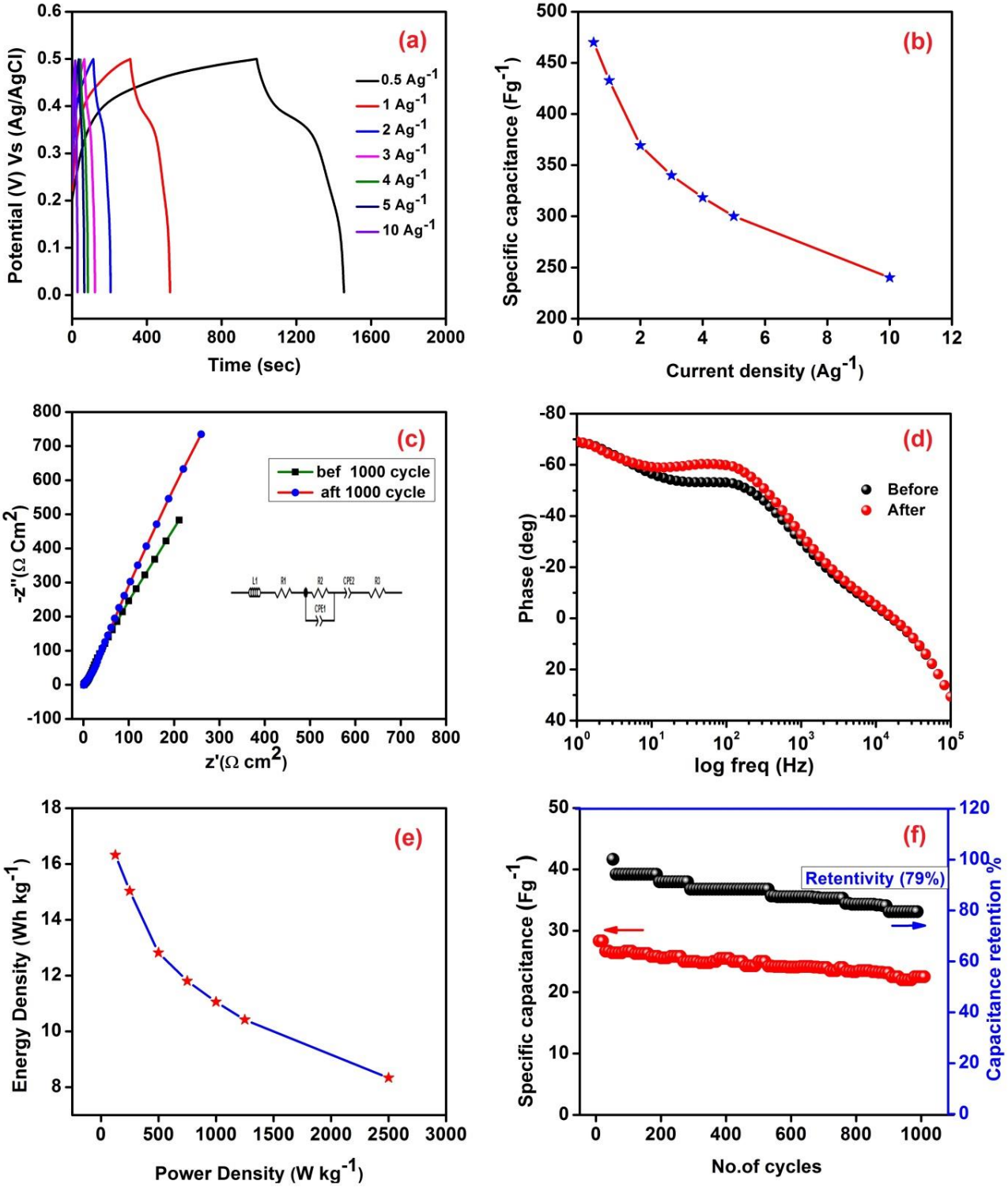
(a)
Potential (V) Vs (Ag/AgCl)
Time (sec)
0.5 Ag-1
1 Ag-1
2 Ag-1
3 Ag-1
4 Ag-1
5 Ag-1
10 Ag-1
(b)
Specific capacitance (Fg-1)
Current density (Ag-1)
(c)
-z''(Ω Cm2)
z'(Ω cm2)
bef 1000 cycle
aft 1000 cycle
(d)
Phase (deg)
log freq (Hz)
Before
After
(e)
Energy Density (Wh kg-1)
Power Density (W kg-1)
(f)
Specific capacitance (Fg-1)
Capacitance retention %
No.of cycles
Retentivity (79%)

Fig. 12

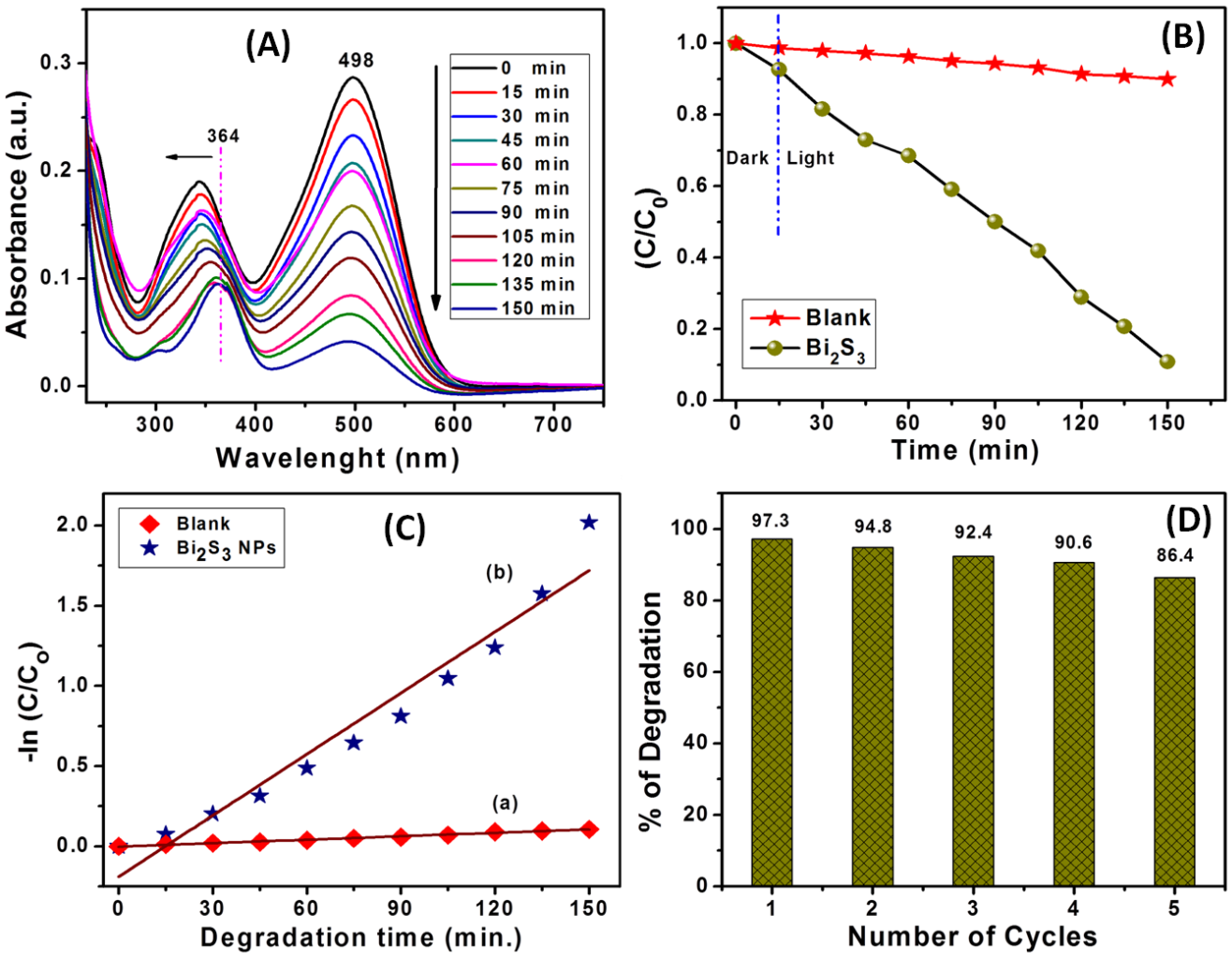
(A)
498
364
0 min
15 min
30 min
45 min
60 min
75 min
90 min
105 min
120 min
135 min
150 min
Absorbance (a.u.)
Wavelenght (nm)
(B)
Dark
Light
Blank
Bi2S3
(C/C0)
Time (min)
(C)
Blank
Bi2S3 NPs
(b)
(a)
-ln (C/Co)
Degradation time (min.)
(D)
97.3
94.8
92.4
90.6
86.4
% of Degradation
Number of Cycles

Fig. 13

Table 1. Scan rate versus specific capacitance

Scan rate (mVs^{-1})	Specific capacitance (Fg^{-1})
1	202
5	129.4
10	109.2
25	93.4
50	84.1
75	70.5
100	58.2

Table 2. Current density versus specific capacitance

Current density A g^{-1}	specific capacitance F g^{-1}
0.5	470
1	432.8
2	369.2
3	340
4	318.4
5	300
10	240

Table 3. Comparison of Specific capacitance for the same electrode materials with various preparation methods.

Electrode materials	Preparation method	Electrolyte	Potential window (v)	Current density (Ag^{-1})	Specific capacitance (Fg^{-1})	No of cycles	Retentivity %	Reference
Bi_2S_3/RGO	Solvothermal	2M KOH	-1.0 to -0.2	1 Ag^{-1}	290 Fg^{-1}	500	91%	17
Bi_2S_3	Hydrothermal	6M KOH	0 to 0.65	1 Ag^{-1}	233 Fg^{-1}	2000	-	47
Bi_2S_3	Solvothermal	0.1M Na_2So_4	-0.6 to 0.0	1 Ag^{-1}	270 Fg^{-1}	1000	62.5%	48
Bi_2S_3	Hydrothermal	2M KOH	-0.1 to 0.6	1 Ag^{-1}	152.2 Fg^{-1}	1000	87%	49
Bi_2S_3 [thin film]	Silar	1M Na_2So_4	-0.7 to -0.1	1 Ag^{-1}	289 Fg^{-1}	1000	59%	50
Bi_2S_3	Hydrothermal	1M Na_2So_4	-0.7 to -0.1	1mA cm^{-2}	185.7 F cm^{-2}	-	-	51
Bi_2S_3/PbS [thin film]	Silar	0.5M Na_2So_4	-0.7 to 0.0	1 Ag^{-1}	402.4 Fg^{-1}	1000	71%	52
Bi_2S_3	**Solvothermal**	**1M KOH**	**0.0 to 0.6**	**0.5 Ag^{-1}**	**470 Fg^{-1}**	**1000**	**79%**	**Present work**

Table 4. Determined estimations of L1, R1, R2, R3, CPE1 and CPE2 through fitting of the impedance spectra dependent on the equivalent circuit.

Sample	**L_1**	**R_1 (Ω)**	**R_2 (Ω)**	**R_3 (Ω)**	**CPE_1-T(F)**	**CPE_1-P(F)**	**CPE_2-T(F)**	**CPE_2-P(F)**
Bi_2S_3	$8.9093E^{-7}$	0.89	1.966	-0.042974	0.0015924	0.9931	0.0032573	0.70612

Figures

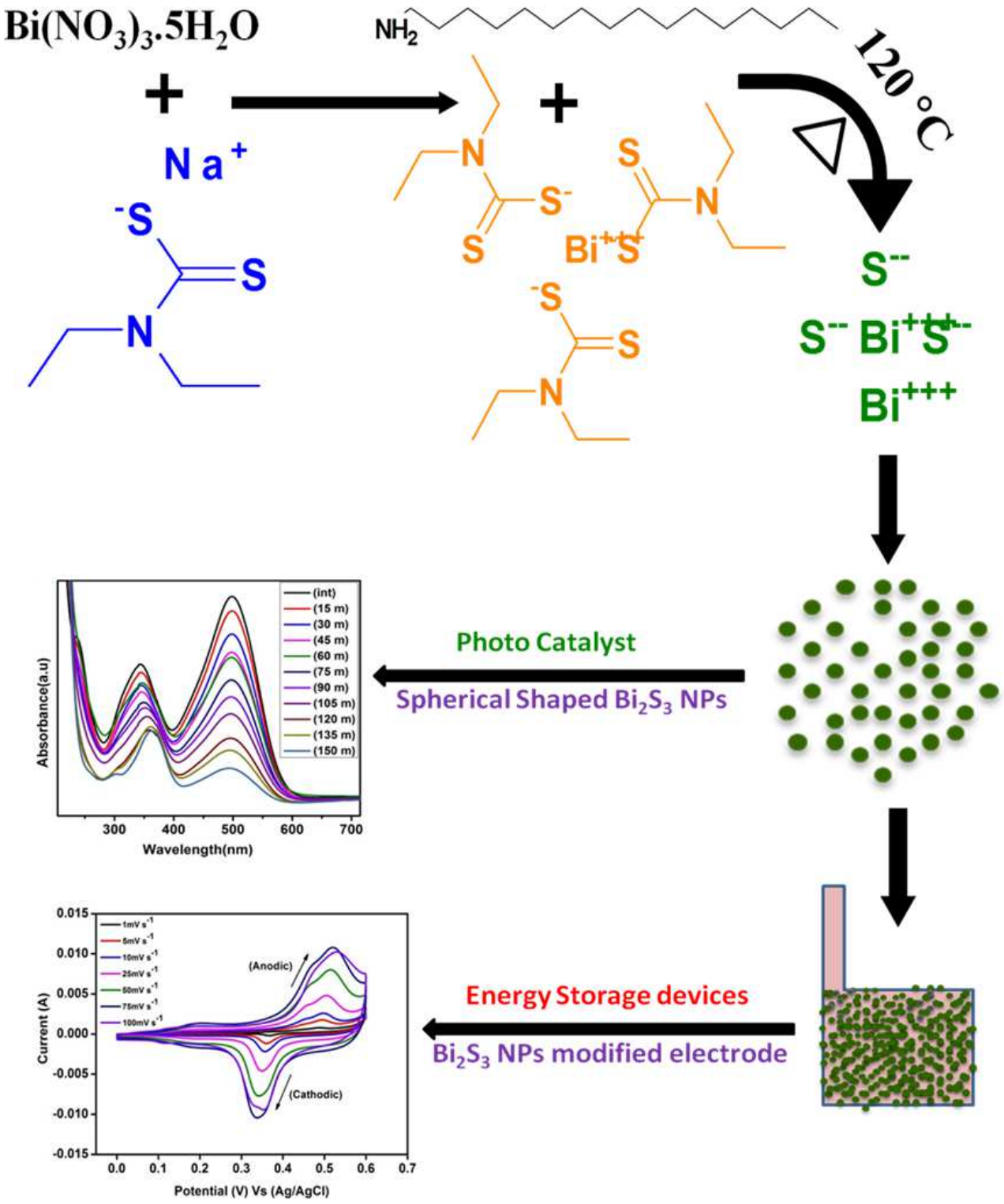

Figure 1

Schematic representation for the Bi2S3 nanoparticles synthesis

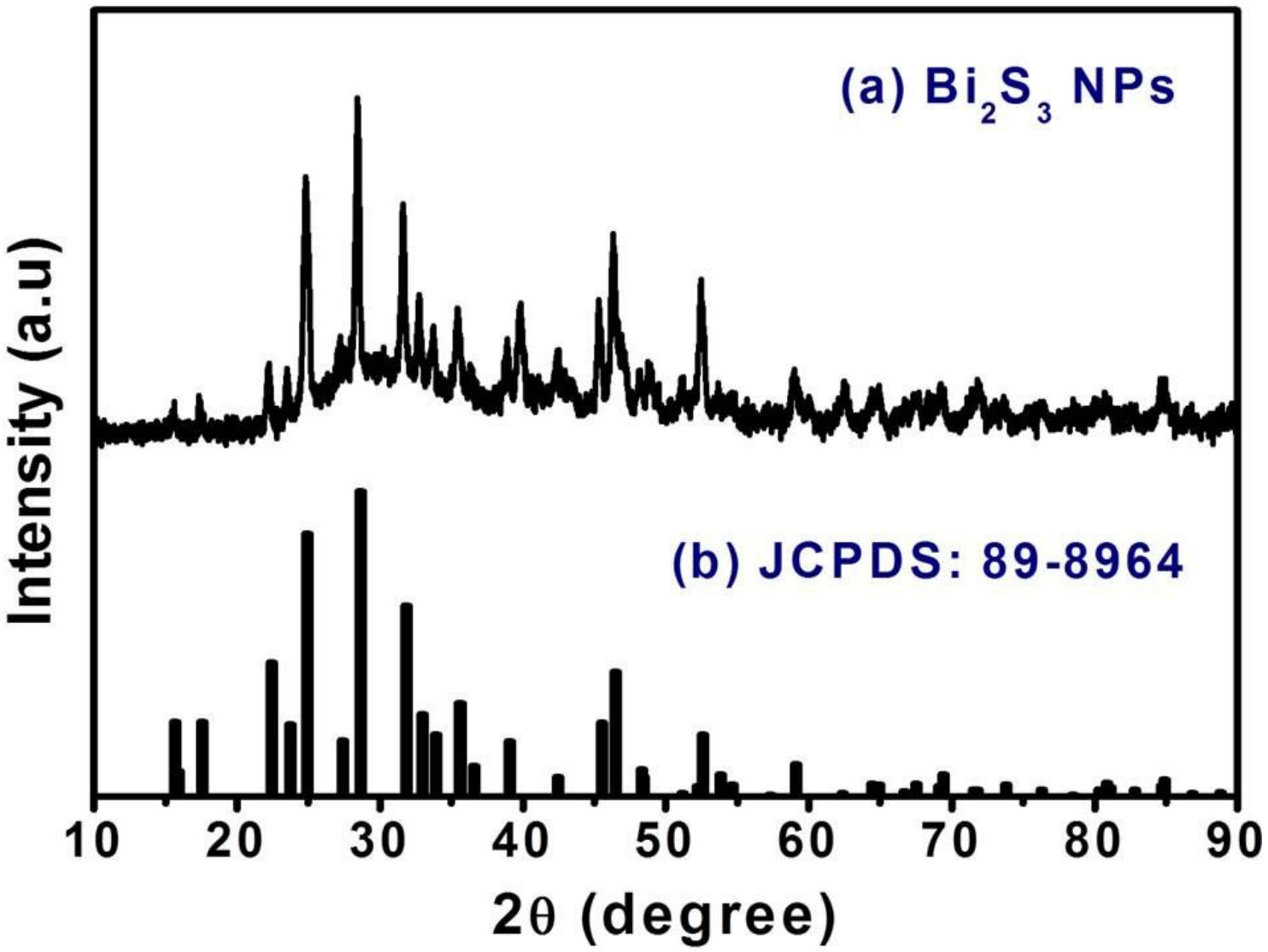

Figure 2

Powder XRD spectrum of as-prepared Bi2S3 nanoparticles

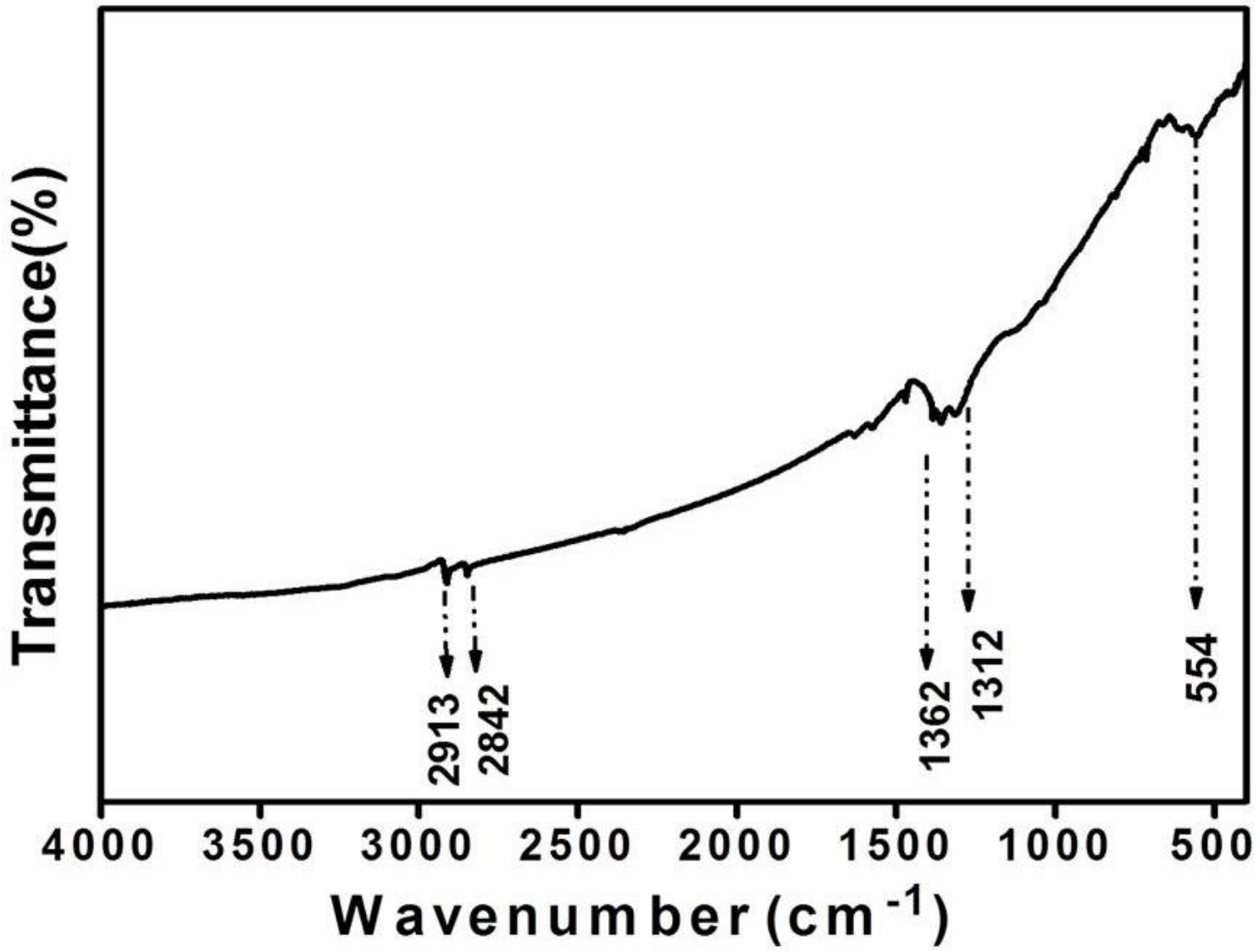

Figure 3

Representative FTIR spectrum of as-prepared Bi2S3 NPs

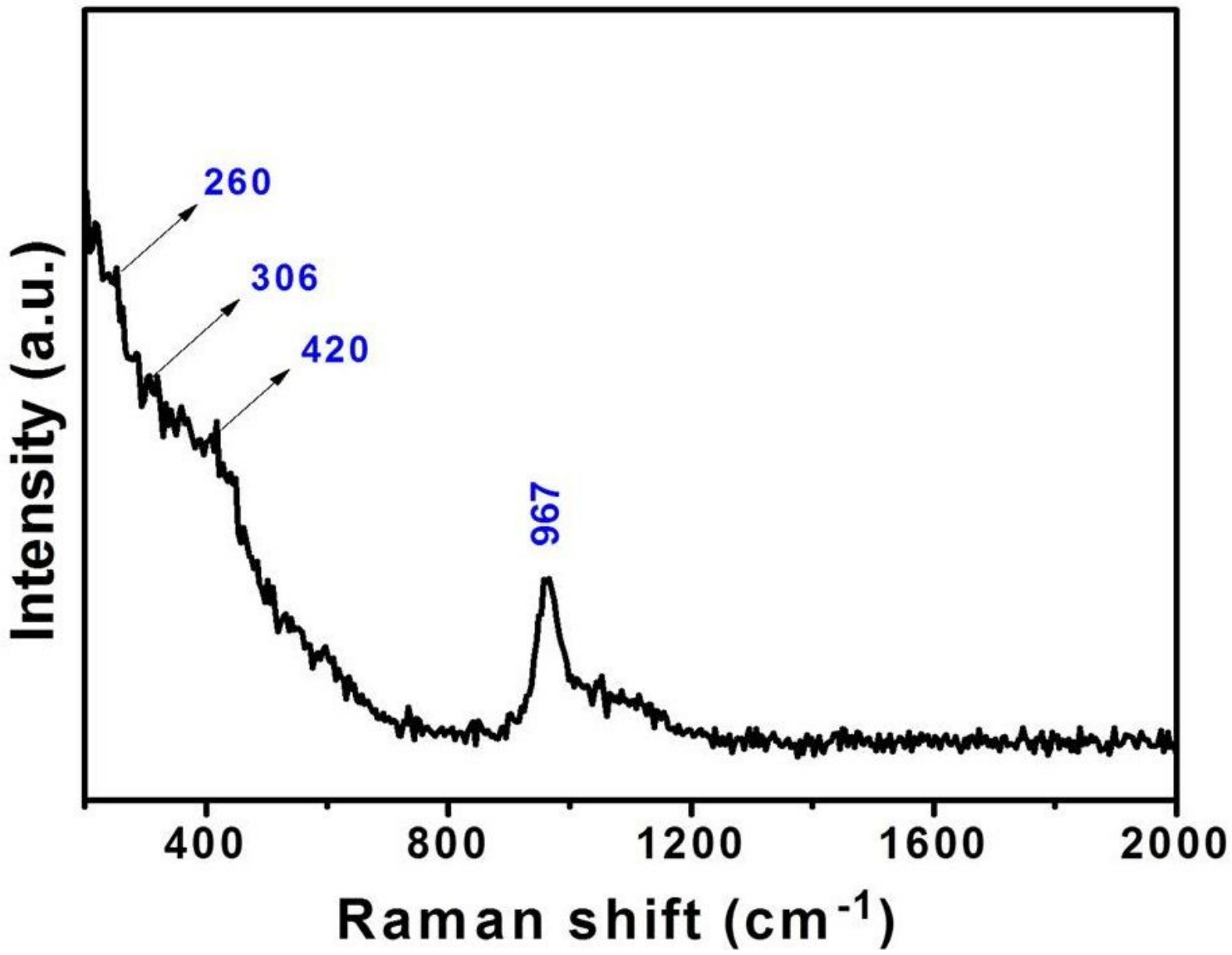

Figure 4

Raman spectrum of as-synthesized Bi2S3 nanoparticles

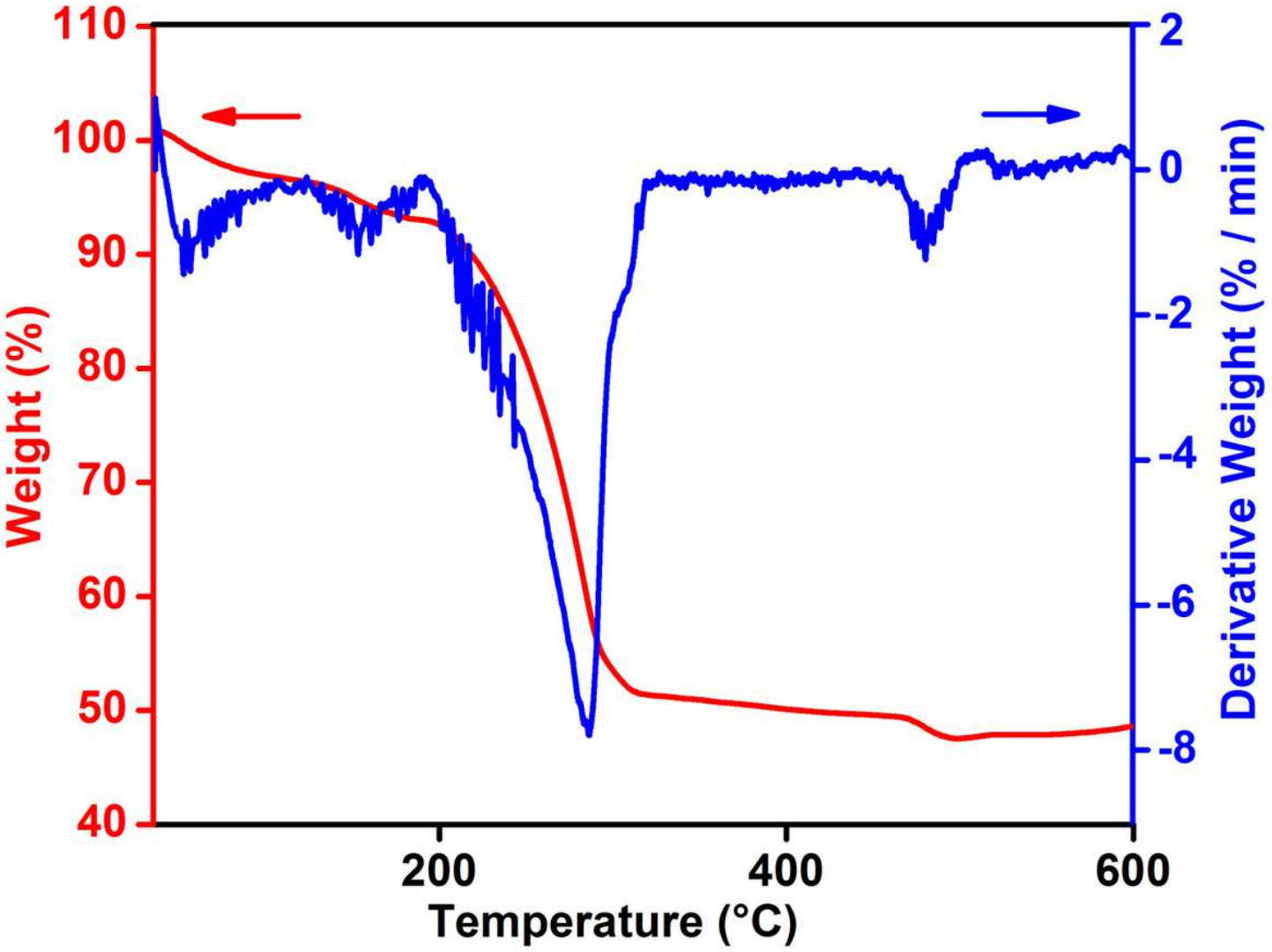

Figure 5

Thermo gravimetric analysis of the Bi[DTC] complex

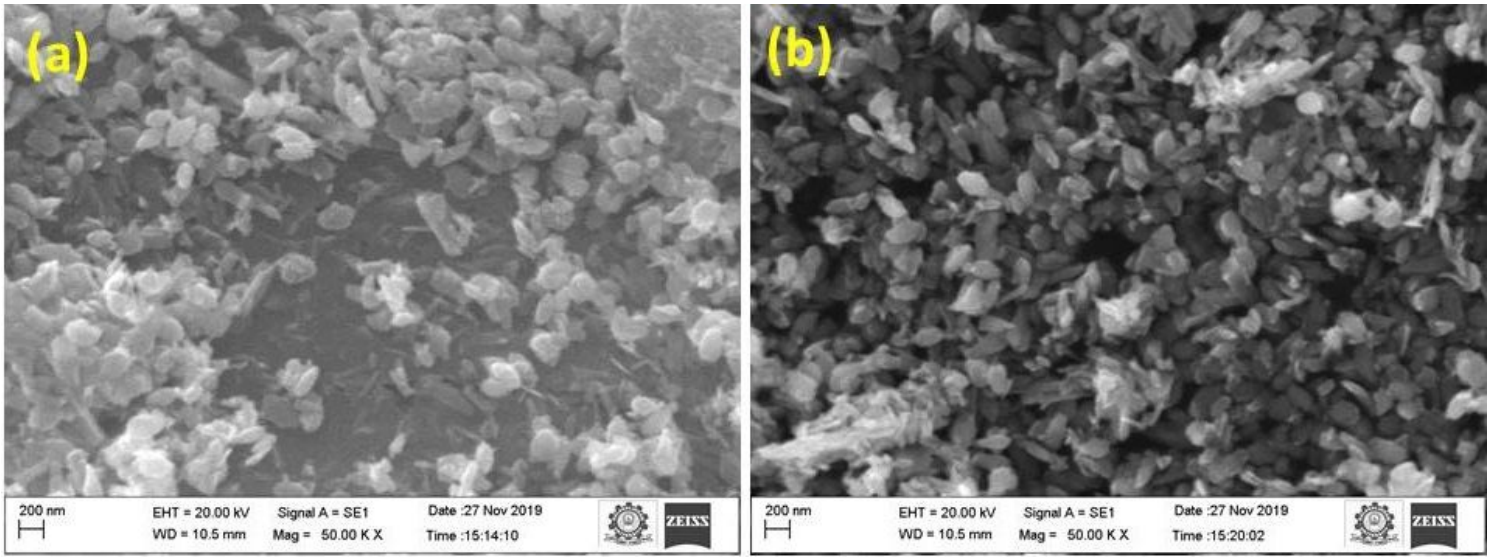

Figure 6

SEM image of synthesized Bi2S3 NPs at 200 nm range

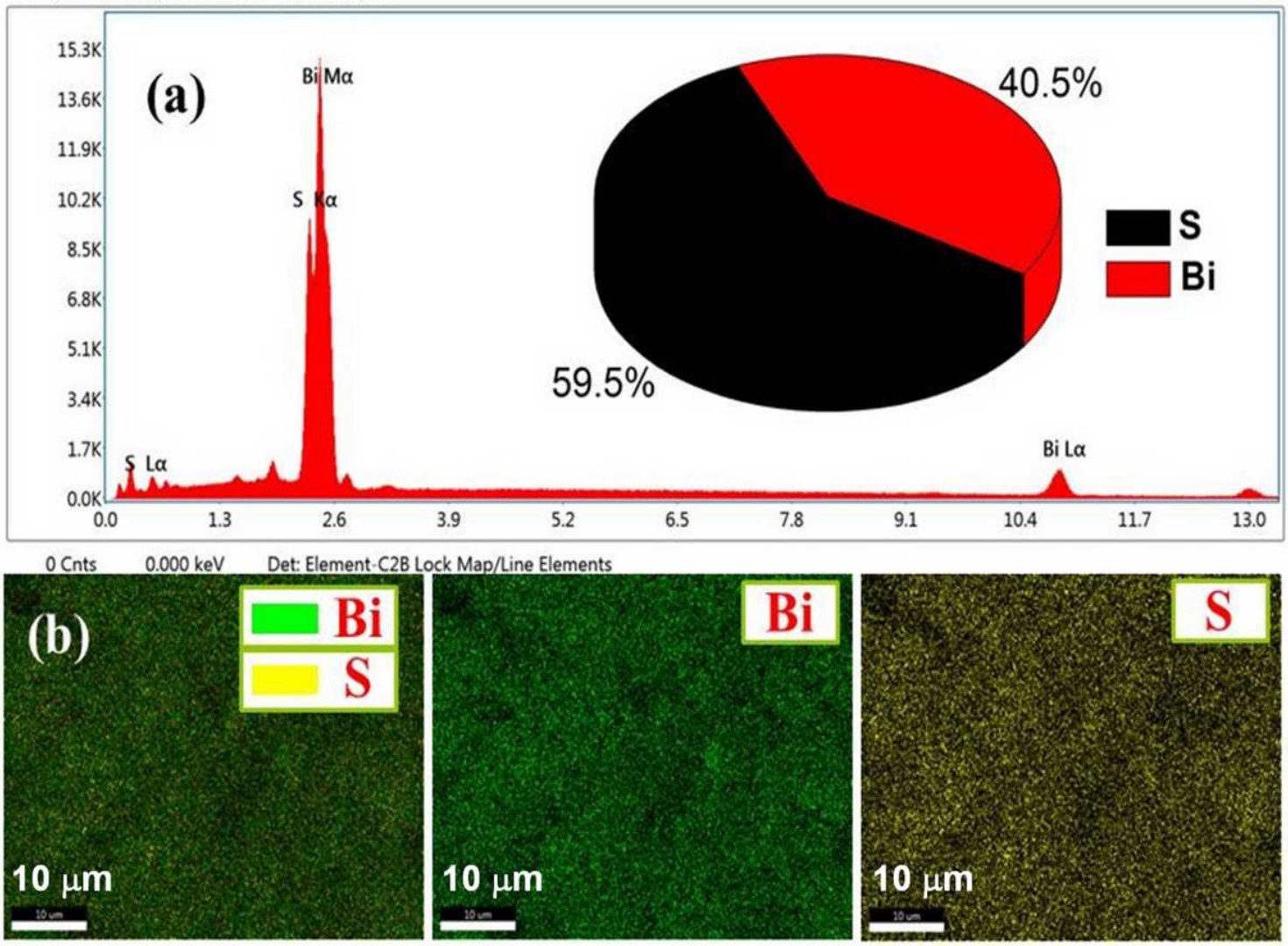

Figure 7

(a) EDS spectrum of Bi2S3 NPs and (b) mapping images of prepared Bi2S3 NPs

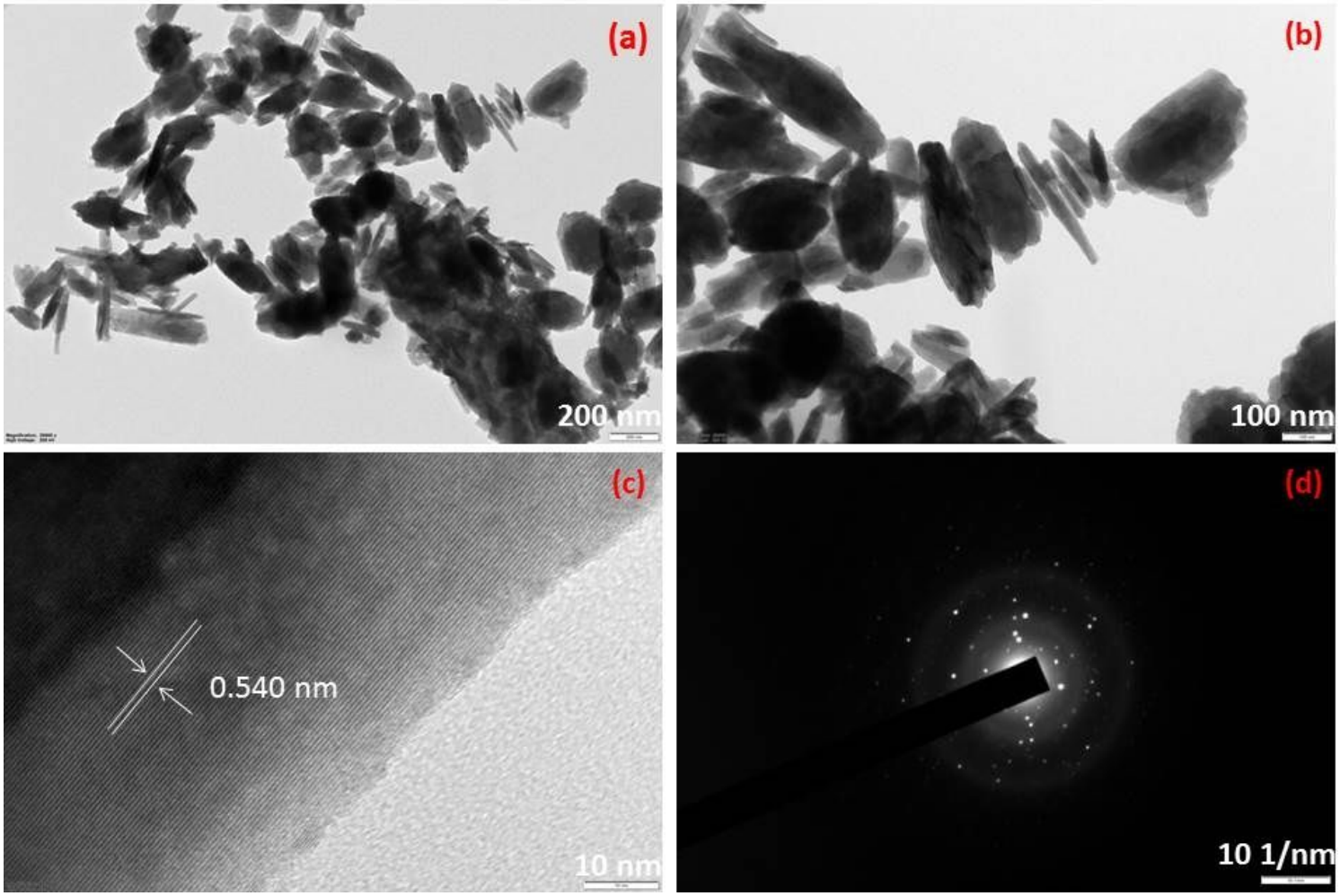

Figure 8

(a-c) HR-TEM analysis with different magnifications and (d) SEAD pattern of Bi2S3 NPs

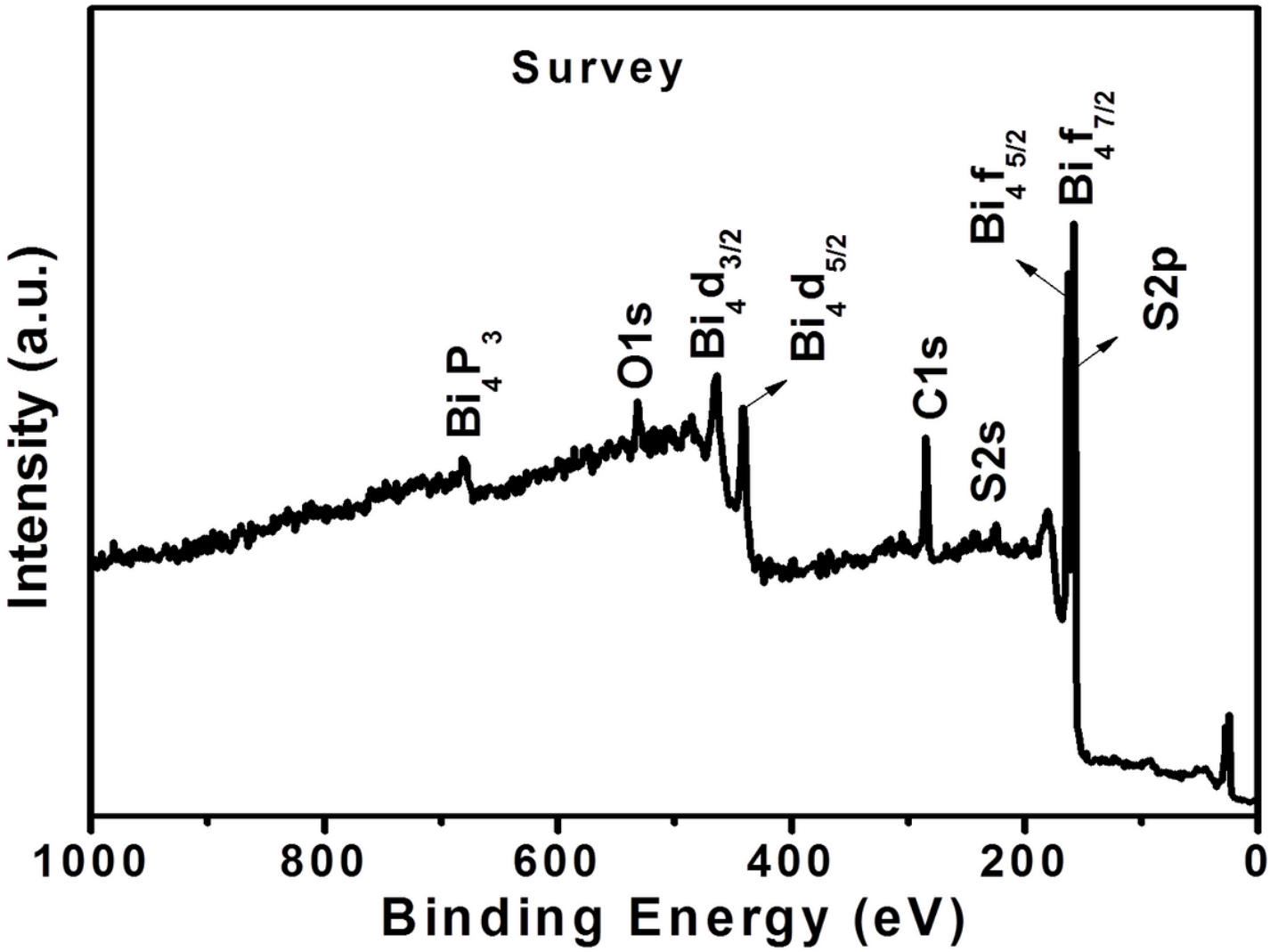

Figure 9

X-ray Photoelectron Spectroscopy full survey spectrum of spherical shaped Bi2S3 NPs

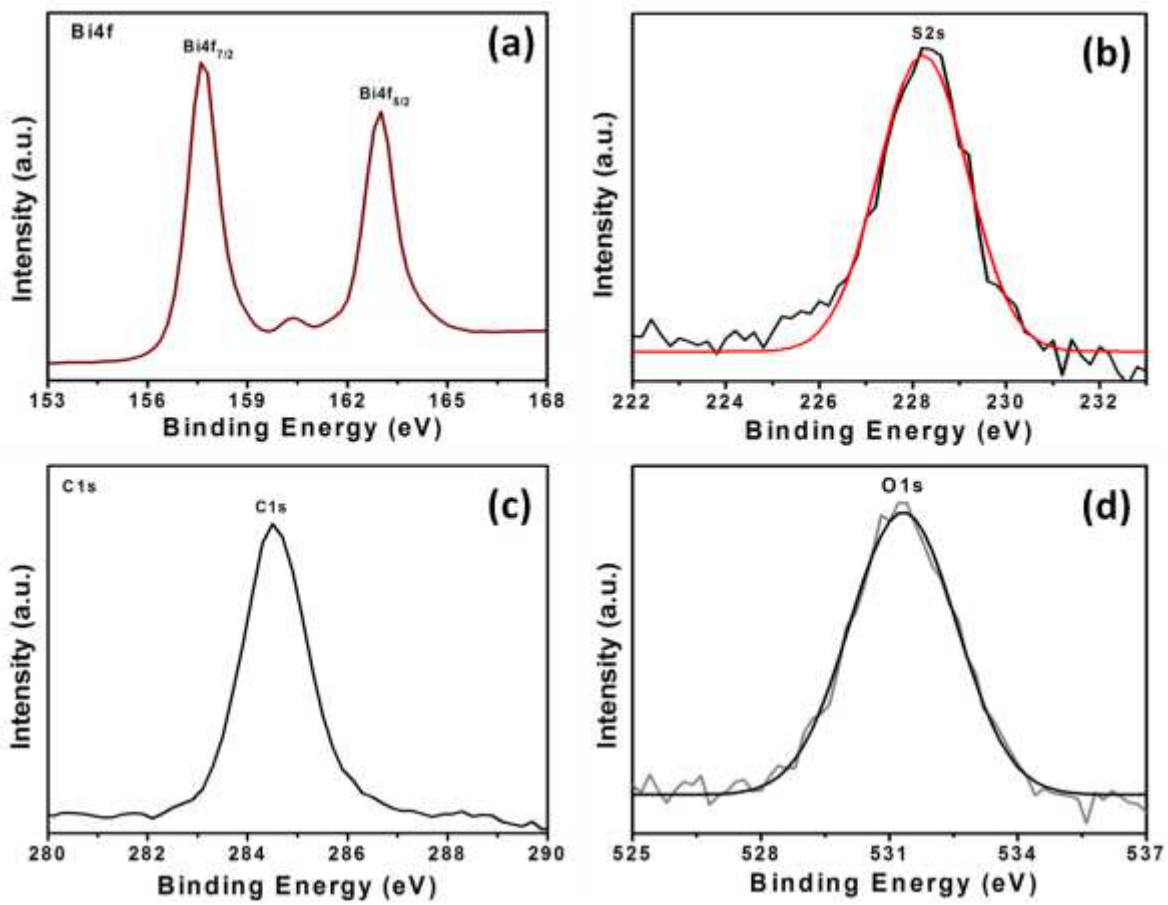

Figure 10

XPS higher resolution spectra of (a) Bi4f (b) S2S (c) C1S (d) O1S

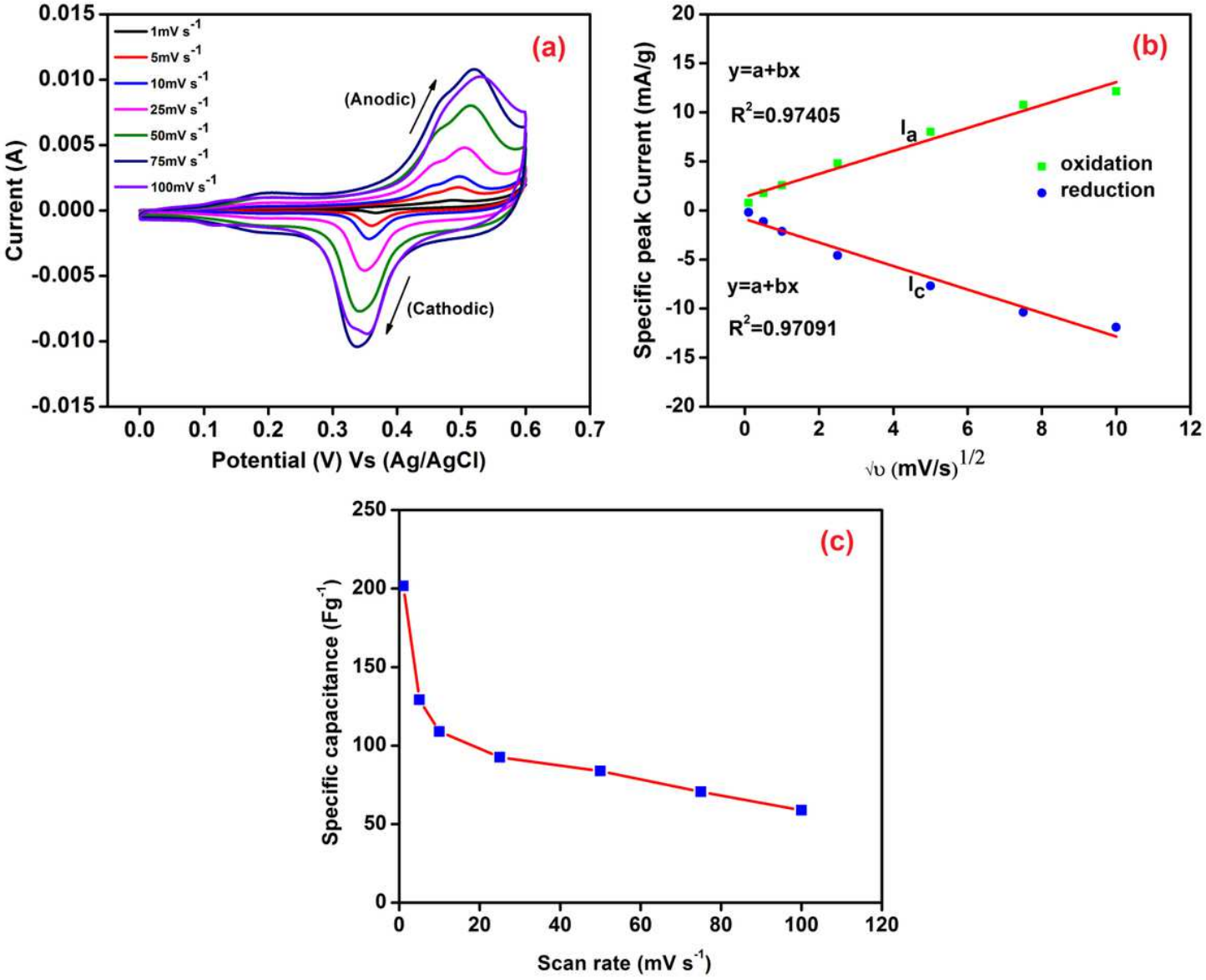

Figure 11

(a) CV curves at different scan rates, (b) Oxidation peak current (Ia) and reduction peak current (Ic) various scan rates, and (c) Specific capacitance vs scan rate

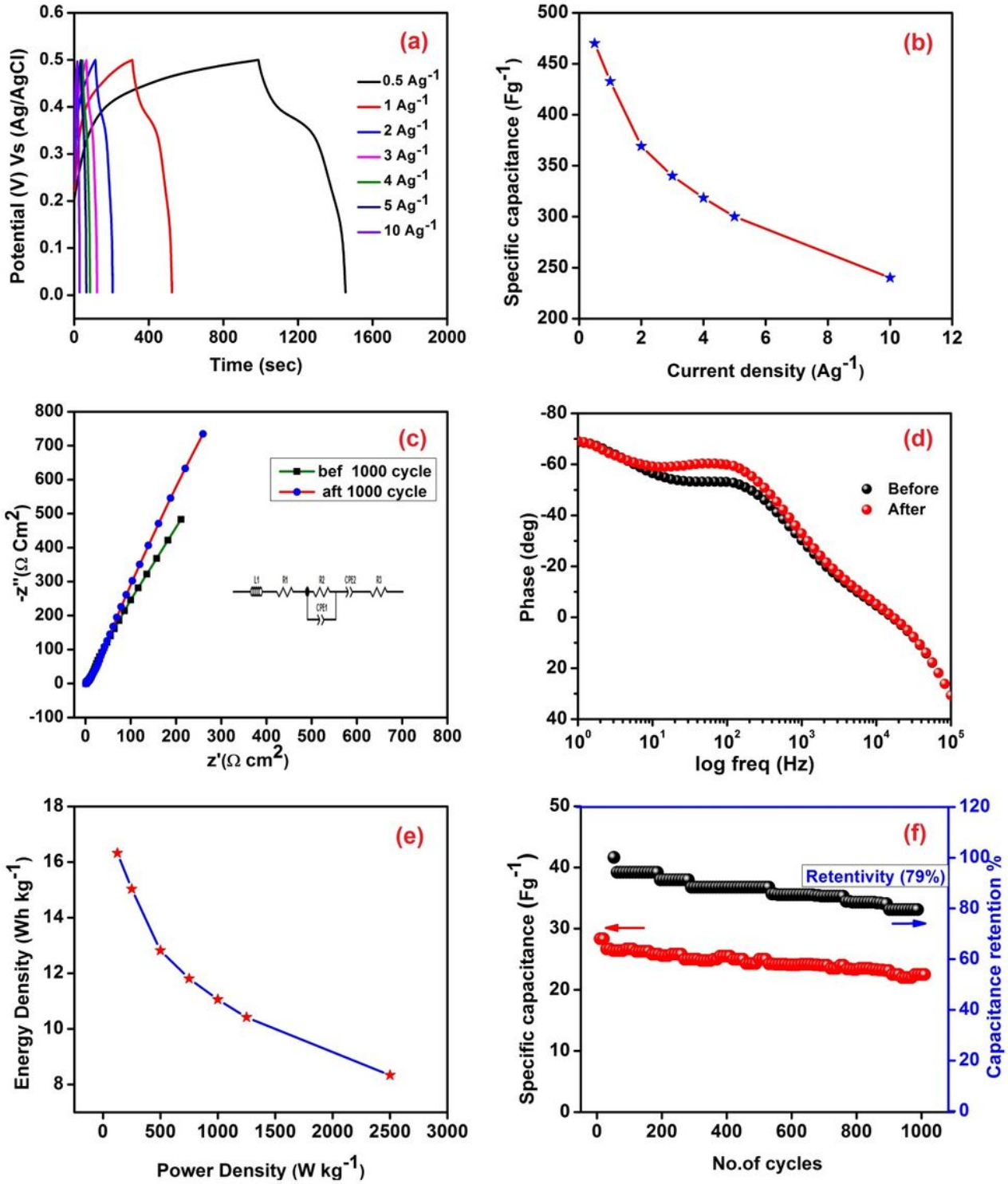

Figure 12

(a) galvanostatic charge-discharge curves at different current densities, (b) Specific capacitance vs current density, (c) EIS spectra, (d) Bode plot for before and after 1000 cycles, (e) Ragone plot related to power densities and energy densities of Bi2S3 NPs, (f) Specific capacitance variation over 1000 charge-discharge cycles at 5 A g-1, and retentivity plot of Bi2S3 NPs

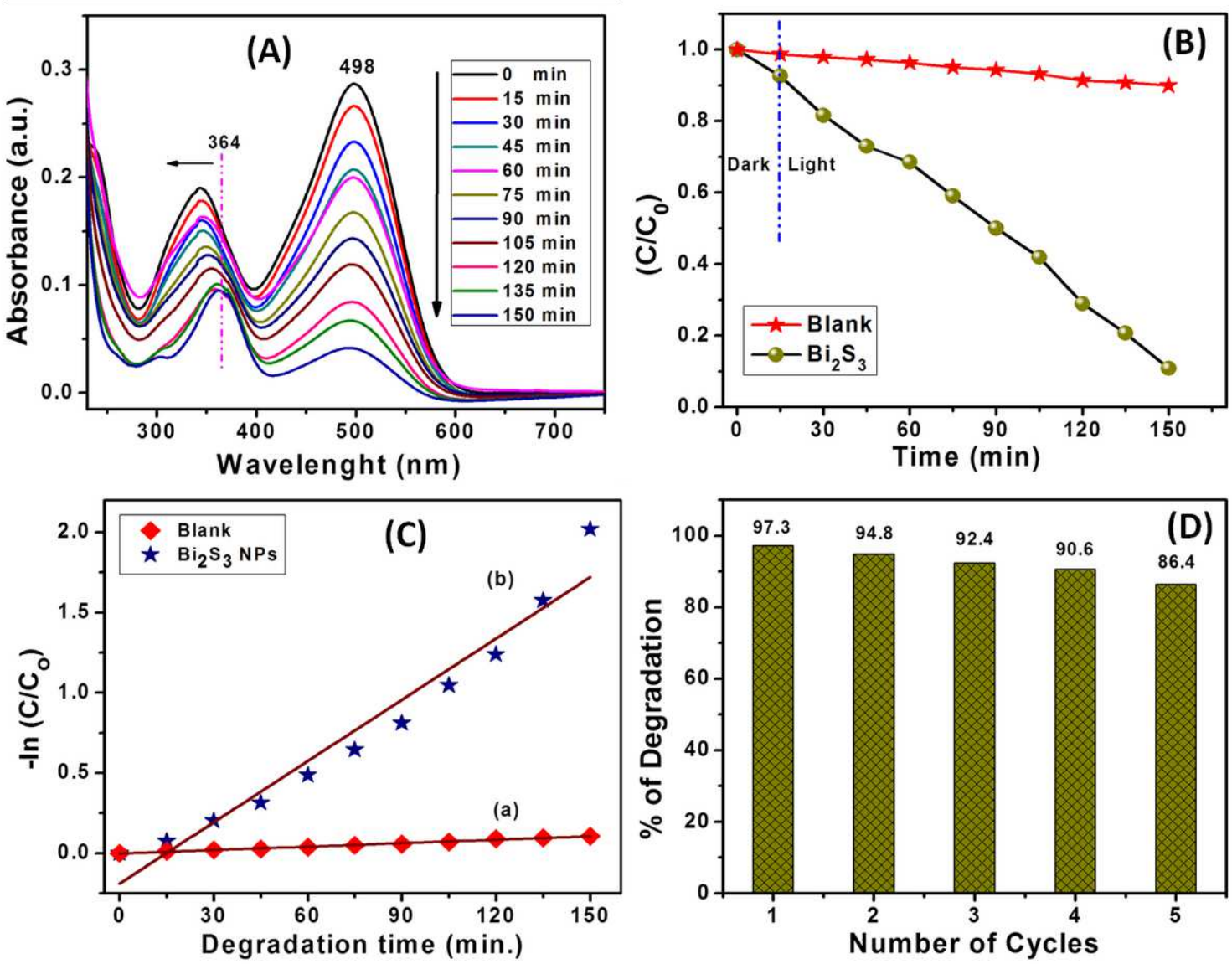

Figure 13

(A) Photocatalytic degradation of Congo Red (CR) dye using Bi2S3 as photocatalyst, (B) Degradation profiles of CR in the presence of Bi2S3 NPs and hierarchical nanostructures (C) Photodegradation calibration plot, (D) recycle efficiency of the photocatalyst, photocatalytic efficiency of the reused Bi2S3 NPs for the degradation of CR dye